Outflows, Mergers, and Tori, Oh My!

by

Steven Fahlman

A thesis submitted in partial fulfillment of the requirements for the degree of

Master of Science

Department of Physics
University of Alberta

Abstract

We study long-term evolution of accretion tori around hypermassive neutron stars in the context of neutron star merger transients, their involvement in the creation of short gamma-ray bursts, and their role in the synthesis of the heaviest elements in the universe. First we conduct 2D axisymmetric hydrodynamic simulations with selected initial conditions relevant to the neutron star merger GW170817, and compare our ejected masses and velocities to those inferred from standard two-component kilonova modeling of the event. Our suite of microphysics includes neutrino transport, nuclear recombination, and a viscous parameterization of magnetic stresses. We find that these are not sufficient to drive the ejected blue mass of the kilonova to velocities of $0.3c$ required by standard kilonovae fits, motivating the need for including full 3D magnetohydrodynamics in simulations. As an initial step to implementing this, we modify the unsplit solver in the `FLASH` code to evolve hydrodynamics in 3D spherical coordinates. Tests of the code are demonstrated via the initialization and evolution of a Sedov blast wave and a 3D equilibrium torus.

Preface

This thesis is an original work by Steven Fahlman. Chapter 2 of this thesis was published in the Astrophysical Journal as 'Fahlman, S. & Fernández, R. 2018, "Hypermassive Neutron Star Disk Outflows and Blue Kilonovae", ApJL, 869, L3', ©AAS, reproduced with permission. For this thesis, the introduction of "Hypermassive Neutron Star Disk Outflows and Blue Kilonovae" has been removed, and a new short introduction to Chapter 2 was instead put in its place. The rest of the text in Chapter 2 (section 2.1 and onwards) appears exactly as it was published aside from minor typo fixes and the addition of a footnote. Dr. Fernández proposed the idea for the project, and originally customized the `FLASH` code to include the microphysics and geometry required to evolve tori in the post-merger environment. I made minor modifications and bug fixes to the equation of state necessary for the code to function with high density tori. I ran the simulations and performed post processing using scripts of my own and also some that were suitably modified for the new parameter space, but originally provided by Dr. Fernández. I wrote the first working draft of the manuscript and figures, which was subjected to heavy edits by Dr. Fernández and myself.

Acknowledgements

I would like to thank the continued support, guidance, war tactics, and life saving abilities of my supervisor, Rodrigo Fernández. My thanks also to the other members of our research group, Coleman Dean and Mario Ivanov, who occasionally provide useful insights amidst the general inanity of our conversations. My condolences also to my family and especially my fiancée, who have to feign interest for hours while I blabber about my work.

Contents

List of Tables

List of Figures

Abbreviations

AMR Adaptive Mesh Refinement

BH Black Hole

CCSN Core Collapse Supernova

CFL Courant-Friedrichs-Lewy condition

EM Electromagnetic

EOS Equation of State

GRMHD General Relativistic Magnetohydrodynamics

GW Gravitational Wave

HD Hydrodynamics

HMNS Hypermassive Neutron Star

ISCO Innermost Stable Circular Orbit

MHD Magnetohydrodynamics

MRI Magnetorotational Instability

NR Newton-Raphson iterations

NS Neutron Star

PLM Piecewise Linear MUSCL-Hancock method

sGRB short Gamma-Ray Burst

SMNS Supermassive Neutron Star

Chapter 1

Introduction to Neutron Star Mergers

The story of neutron star mergers began long ago in the dark ages of astronomy (circa 2000) when there were two large unexplained questions in astrophysics: "What is the origin of the extremely energetic and elusive short gamma-ray bursts?", and "Where do the heaviest elements in the universe come from?".

For the latter, it had long been proposed that the ejected material from neutron star (NS) mergers could provide the hot, neutron-rich environment necessary for elements to undergo rapid neutron capture (r-process) and create the heaviest elements (Lattimer and Schramm, 1974). The r-process was defined by Burbidge et al. (1957), where the authors noted that when neutron captures onto a seed nucleus occur at a rapid rate relative to the β-decay processes ($\sim 0.01 - 10$ s), it is possible to form the most neutron-rich nuclei, which lie along the neutron drip line. At this point, it becomes energetically unfavourable to add neutrons, and the nuclei are unstable to inverse β-decay. This increases the ratio of protons to neutrons, allowing for the addition of more neutrons, and the r-process chain continues. The elements created by the r-process are unstable, and were thought to primarily be formed in the neutron-rich tidal tails as the two NSs coalesce. Owing to their instability, the nuclei radioac-

tively decay over a broad range of timescales, injecting energy into the system that thermalises to create a detectable electromagnetic transient on a similar timescale (Li and Paczyński, 1998; Kulkarni, 2005). Advancements in nuclear theory, in particular research into the effects of radioactive heating (Metzger et al., 2010) and the opacities of elements heavier than iron (Kasen et al., 2013; Barnes and Kasen, 2013; Tanaka and Hotokezaka, 2013), led to a detailed model of *kilonovae*: Radioactively powered transient light curves observable at both infrared ("red") and optical/UV ("blue") wavelengths (Metzger et al., 2010; Kasen et al., 2017; Metzger, 2017). The exact extent of the contribution from NS mergers to the r-process abundance in the universe compared to the extent of contributions from other sources like core-collapse supernovae (CCSN) is still an active area of research (Côté et al., 2018; Hotokezaka et al., 2018; Siegel et al., 2019).

The idea of compact object mergers providing the engine for short gamma-ray bursts (sGRBs) was also proposed in the last few decades (Paczynski, 1986; Eichler et al., 1989). Such bursts require $\gtrsim 10^{51}$ ergs of energy to be deposited into a small area on the short timescale of $\sim 10-100$ ms, feasible to accomplish in a NS merger, and estimates of merger rates at the time were promising compared to the incident rate of sGRBs (Eichler et al., 1989; Narayan et al., 1992). Theory states that material from the newly formed accretion torus around the central object accelerates to ultra-relativistic velocities (Lorentz factors $\gtrsim 100$), powering the release of γ-rays. The energy must be extracted from an as yet indeterminate central engine: accretion, neutrinos, magnetar strength magnetic stresses, or a combination of the three (Nakar, 2007; Berger, 2014; Paschalidis, 2017; Metzger et al., 2018).

In addition to the above questions, the inspiral of two compact objects provides an environment where general relativistic effects are present, including the creation of gravitational waves (GWs). The construction and subsequent detection of GWs from numerous binary black hole (BH) mergers by the

LIGO/VIRGO detectors allowed us to test theories of general relativity against numerical relativity simulations (e.g., Abbott et al. 2016).

When at least one NS is involved in the merger, mass can be ejected, unlike binary BH mergers. In these cases, it is then possible to place constraints on the equation of state of nuclear matter. From the GW signal we can infer tidal effects through the tidal deformability parameter, which depends on the mass and radius of the star (Abbott et al., 2017b; De et al., 2018). Additional constraints can be placed on the EOS when the accompanying EM kilonova is detected coincident with the GW signal (Radice and Dai, 2019; Margalit and Metzger, 2019). The discovery of a signal in both gravitational and electromagnetic waves from the first binary NS merger, GW170817 (Abbott et al., 2017b), conforms to the general predictions of a kilonova, providing strong evidence for r-process element formation in NS mergers.

1.1 Kilonovae, GW170817, and You

The kilonova is thought to result from the radioactive decay of elements formed during the r-process, as the hot, neutron-rich, and sub-relativistic environment of the merger provides correct conditions for the r-process to occur (Li and Paczyński, 1998; Just et al., 2015; Lippuner et al., 2017). The neutron-rich dynamical ejecta is unbound from the system via tidal forces and shock heating during the final stages of inspiral. It is ideal for the formation of heavy elements, including lanthanides and actinides, which have high opacities to photons, $\sim 10\ \mathrm{cm}^2\ \mathrm{kg}^{-1}$, due to the forest of absorption lines in open d-shell elements (Kasen et al., 2013; Hotokezaka et al., 2013; Radice et al., 2018). The light curve from the decay of lanthanides/actinides peaks in the infrared over a timescale of days to weeks, informally called a "red kilonova". Matter that does not coalesce into the central compact object and remains marginally bound will form an accretion torus around the merger, comprising $\lesssim 10\%$ of the

system's total gravitational mass. On a thermal timescale ($\sim$ 1 s), the torus will evaporate due to accretion and energy deposition from neutrinos, nuclear recombination, and magnetic stresses, driving outflows sometimes referred to as disk winds (Fernández and Metzger, 2013; Metzger and Fernández, 2014; Perego et al., 2014; Just et al., 2015; Lippuner et al., 2017; Fujibayashi et al., 2018; Fernández et al., 2019). Since the timescale for evaporation is longer than that of neutrino interactions, the neutron-richness of these outflows varies as weak interactions with neutrinos drive the electron fraction toward equilibrium. A higher electron fraction (or lower neutron-richness), inhibits heavy r-process element formation and the opacity of the material is closer to ~ 1 cm^2 kg^{-1}, causing an earlier ($\sim$ days) peak in the light curve, called a "blue kilonova".

The type of merger remnant modifies the kilonova. Depending on the total mass of the merger, the object formed is predicted to be a uniformly rotating stable NS, a differentially-rotating, unstable hypermassive NS (HMNS), or a BH (Margalit and Metzger, 2019). When the gravitational mass is less than the supermassive limit, $\sim 1.2\,M_{\rm TOV}$, where $M_{\rm TOV}$ is the maximum mass supported by a cold irrotational Tolman-Oppenheimer-Volkoff configuration, the object is most likely an indefinitely lived supermassive NS (SMNS) (Baumgarte et al., 2000; Paschalidis et al., 2012; Kaplan et al., 2014). A SMNS is theorized to deposit additional energy in the form of neutrino emission and rotational kinetic energy associated with its steady spin down to the irrotational TOV configuration into the torus (Fujibayashi et al., 2018).

In the case where the total gravitational mass of the binary NS system is above the uniformly rotating maximum mass ($\sim 1.2\,M_{\rm TOV}$) and below the hypermassive limit, $\sim 1.4\,M_{\rm TOV}$ (where the exact limit is EOS dependent), the remnant left behind is likely a HMNS, which is a NS supported against gravitational collapse by differential rotation and thermal pressure (Baumgarte et al., 2000; Kaplan et al., 2014; Hanauske et al., 2017; Espino et al., 2019). Provided it does not collapse from dynamical instabilities, a HMNS is thought

to be unstable on a secular timescale ($\sim$ ms, Kaplan et al., 2014) and loses energy through angular momentum transport via the magnetorotational instability (MRI, Hawley and Balbus, 1991), magnetic winding, (Duez et al., 2006), neutrino emission (Palenzuela et al., 2015; Sekiguchi et al., 2015), and emission of GWs (Shibata et al., 2005; Ruiz et al., 2019). The hot, neutron-rich HMNS is a strong emitter of neutrinos ($L_\nu \sim 10^{52}$ ergs/s), driving neutrino powered winds and making the resulting kilonova bluer. In the case of prompt BH formation, when the total mass exceeds the hypermassive limit, all neutrino flux is generated predominantly via electron capture in the high density and temperature regions of the torus. This neutrino self-irradiation is much weaker than that in the HMNS case. Magnetohydrodynamic stresses (e.g., Blandord-Znajek mechanism, inertial frame dragging) and neutrino annihilation are primary contenders for launching a relativistic jet, as a baryon free funnel is formed in the polar regions of the BH (Blandford and Znajek, 1977; Berger, 2014). This has observational implications, not only for the additional acceleration of sub-relativistic matter, but also for providing a chance to discriminate between the central engines powering sGRBs.

The kilonova of GW170817 peaked after $\lesssim 2$ days in the optical, and reddened on a timescale of days to a week (Villar et al., 2017; Cowperthwaite et al., 2017; Drout et al., 2017), consistent with a remnant HMNS surviving for a finite lifetime. Energy deposition from the spin down of a infinitely long lived supermassive NS would result in velocities, electron fraction, and mass ejecta higher than that inferred from GW170817, while the formation of a prompt BH is unlikely for the opposite reasons (Metzger, 2017; Foucart et al., 2019; Margalit and Metzger, 2019). While neither of these cases have been ruled out entirely (Margalit and Metzger, 2017, 2019; Miller et al., 2019), we focus our efforts on the most probable outcome: A HMNS that survives for longer than a dynamical timescale.

GW170817 is the first opportunity to compare our simulations of binary

NS mergers with observational data from a merger event. The chirp mass, a measure of the total system mass by GW observations, is constrained to be $2.78^{+0.05}_{-0.03}\,M_\odot$ (Abbott et al., 2017b). Standard kilonova models using a two component (red and blue) fit to the light curve return observed outflow velocities and masses of $0.15c$ and $0.02 - 0.05\ M_\odot$ for the red kilonova, and a blue component with $\sim 0.02\ M_\odot$ moving in the range $0.1c - 0.3c$ (e.g., Villar et al. 2017).

As the majority of ejecta mass ($\sim 80\%$) in GW170817 is thought to arise from post-merger outflows sourced in the accretion torus (e.g., Villar et al. 2017; Metzger 2017), the purpose of this thesis is to characterize that ejecta channel using numerical simulations. In particular we focus on the case of HMNS formation, since modeling of GW170817 favours HMNS formation (Margalit and Metzger, 2017; Shibata et al., 2017a), and is thought to be the outcome in $\sim 50\%$ of mergers (Margalit and Metzger, 2019). We will explore the effects of a HMNS on the post-merger ejecta masses, velocities, and electron fractions, using GW170817 as our benchmark.

Chapter 2

Hypermassive Neutron Star Disk Outflows and the Blue Kilonova of GW170817

Since the dominant ejecta channel for systems like GW170817 is expected to be post-merger outflows from the surrounding torus, we wish to run long-term simulations ($\sim$ 10 s) that include the dominant microphysical effects. To this end, we carry out axisymmetric hydrodynamic simulations including a leakage neutrino transport scheme, viscous treatment of magnetic angular momentum transport, and nuclear recombination of alpha particles. Previous hydrodynamic simulations either do not explore a parameter space relevant to GW170817 (Lippuner et al., 2017; Metzger and Fernández, 2014, hereafter MF14), do not include explicit angular momentum transport (Dessart et al., 2009; Perego et al., 2014), or included a stable long-lived HMNS (Fujibayashi et al., 2018). The velocities and masses extracted from light curve modeling of GW170817 allows us to parameterize for the first time how well our simulated torus outflows can recreate the kilonova, and the sensitivity of the kilonova to physical unknowns (e.g., system/torus mass, neutrino luminosity, HMNS lifetime).

2.1 Methods

Disk outflow simulations use the same approach as in MF14, with updates reported in Lippuner et al. (2017). Below is a brief summary of the computational setup.

2.1.1 Numerical Hydrodynamics

Simulations are carried out using `FLASH3` (Fryxell et al., 2000; Dubey et al., 2009) with suitable modifications (Fernández and Metzger 2013; MF14). The code solves the equations of hydrodynamics and lepton number conservation in axisymmetric (2D) spherical polar coodinates (r, θ) with azimuthal rotation. Gravity, azimuthal shear viscosity, and neutrino emission/absorption are included as source terms. We use the equation of state of Timmes and Swesty (2000) with abundances of neutrons, protons, and alpha particles in nuclear statistical equilibrium, and accounting for the nuclear recombination energy of alpha particles.

Gravity is modeled with the pseudo-Newtonian potential of Artemova et al. (1996), azimuthal shear viscosity follows an α-prescription (Shakura and Sunyaev, 1973), and neutrino effects are modeled with a leakage scheme for emission and annular light bulb for absorption (Fernández and Metzger 2013; MF14). We only include charged-current weak interactions on nucleons. See Richers et al. (2015) for a comparison of this scheme with Monte Carlo neutrino transport.

The computational domain is discretized radially using logarithmic spacing with 128 cells per decade in radius, and using 112 cells equispaced in $\cos\theta$ covering the range $[0, \pi]$.

The HMNS is modeled as a reflecting[1] inner radial boundary at $r = R_{\rm NS}$,

[1]The use of a reflecting boundary preserves the pressure feedback that would be felt via subsonic accretion onto the HMNS. Use of an absorbing boundary would supress this effect.

Table 2.1: Simulation parameters and results. Columns from left to right show model name, central object mass, HMNS radius, initial torus mass, radius of initial torus density maximum, initial HMNS neutrino luminosity ($L_{\nu_e} = L_{\bar{\nu}_e}$), initial torus electron fraction, HMNS lifetime, viscosity parameter, initial torus entropy, ejected mass with positive energy in lanthanide-rich ($Y_e < 0.25$, subscript R for red) and lanthanide-poor ($Y_e > 0.25$, subscript B for blue) material, and mass-averaged velocity of ejected red and blue material.

Model	$M_{\rm NS}$ ($M_\odot$)	$R_{\rm NS}$ (km)	$M_{\rm t}$ ($M_\odot$)	$R_{\rm t}$ (km)	$L_{\nu e}$ (ergs)	Y_e	$\tau_{\rm NS}$ (ms)	α	s ($k_{\rm B}$/baryon)	$\bar{\rm M}_{\rm R}$ ($M_\odot$)	$\bar{\rm M}_{\rm B}$ ($M_\odot$)	$\bar{\rm v}_{\rm R}$ (c)	$\bar{\rm v}_{\rm B}$ (c)
base	2.65	20	0.10	50	$2 \cdot 10^{52}$	0.10	10	0.05	8	0.010	0.023	0.091	0.038
α10								0.10		0.008	0.035	0.135	0.070
α03								0.03		0.007	0.019	0.066	0.032
t01							1			0.013	0.008	0.037	0.039
t30							30			0.002	0.058	0.159	0.093
M2.7	2.70						10	0.05		0.009	0.023	0.097	0.042
M2.6	2.60									0.011	0.018	0.080	0.041
mt03	2.65		0.30							0.049	0.031	0.049	0.039
mt02			0.20							0.029	0.033	0.065	0.030
rt60			0.10	60						0.014	0.013	0.057	0.039
rs30		30		50						0.016	0.009	0.042	0.041
L53		20			$2 \cdot 10^{53}$					0.001	0.041	0.187	0.099
L51					$2 \cdot 10^{51}$					0.013	0.017	0.077	0.039
s10					$2 \cdot 10^{52}$				10	0.020	0.014	0.055	0.033
ye25						0.25			8	0.000	0.033	0.000	0.058
best	2.55	20	0.20	60	$2 \cdot 10^{52}$	0.10	10	0.05	8	0.040	0.022	0.043	0.037

from which prescribed neutrino and antineutrino luminosities are emitted. These luminosities are constant for the first 10 ms, subsequently decaying as $t^{-1/2}$ (MF14). When the HMNS collapses into a BH, the radial boundary becomes absorbing, and the HMNS luminosities are set to zero. The boundary is also moved inward to a position halfway between the innermost stable circular orbit (ISCO) and horizon radii of the newly-formed BH. The computational domain extends out to $r = 2 \times 10^{10}$ cm. The outer radial boundary condition is absorbing, and the boundary conditions in θ are reflecting.

The initial condition for the disk is an equilibrium torus with constant angular momentum, entropy, and electron fraction. The space outside this torus is filled with an inert low-density ambient medium with density in the range $10 - 100$ g cm^{-3} inside $r = 2 \times 10^7$ cm, and decreasing as r^{-2} outside this radius. When collapsing the HMNS into a BH, the cells added to the computational domain are filled with material having the same properties as the surrounding medium, which is immediately accreted. For numerical reasons,

we set a floor of density at $\sim 90\%$ of the initial ambient value.

2.1.2 Model Parameters

The total mass of GW170817 measured from gravitational waves is $2.73^{+0.04}_{-0.01}\,M_\odot$ to 90% confidence (Abbott et al., 2017a). The dynamical ejecta mass expected from numerical relativity simulations is $\lesssim 0.01\,M_\odot$, and disk masses are expected to lie in the range $0.05 - 0.3\,M_\odot$ depending on the equation of state used (e.g., Shibata et al. 2017a). We therefore adopt a baseline model ('base') with HMNS mass $M_{\rm NS} = 2.65\,M_\odot$ and disk mass $M_{\rm t} = 0.1\,M_\odot$.

The radius of the baseline HMNS is taken to be $R_{\rm NS} = 20\,{\rm km}$, following results of numerical relativity simulations (e.g., Hanauske et al. 2017; Shibata and Kiuchi 2017). The lifetime of the baseline HMNS is taken to be $\tau_{\rm NS} = 10\,{\rm ms}$ as a first guess ($\sim$ disk thermal time), with the HMNS luminosities having an initial magnitude of $2 \times 10^{52}\,{\rm erg\,s^{-1}}$ (e.g., Dessart et al. 2009). The HMNS has a surface rotation period of 1.5 ms and we adopt zero spin in the pseudo-Newtonian potential. The HMNS collapses into a BH of the same mass and dimensionless spin 0.8, as typically obtained in numerical relativity simulations (e.g., Shibata et al. 2017a). The inner radial boundary then moves from 20 km to 8.7 km in the baseline model. The magnitude of the α-viscosity is chosen to be $\alpha = 0.05$, following the general relativistic magnetohydrodynamic (GRMHD) results of Fernández et al. (2019). The initial electron fraction and entropy of the baseline disk are $Y_e = 0.1$ and $s = 8\,{\rm k_B}$ per baryon, respectively. All model parameters are summarized in Table 2.1.

We evolve additional models that vary one parameter at a time relative to the baseline simulation, as shown in Table 2.1. We focus on those parameters that are known to have the most impact in the properties of the outflow: lifetime of the HMNS, magnitude of the α-viscosity, magnitude of the HMNS luminosity, mass of the torus and total remnant mass, and radius of the HMNS. Other parameters have a smaller impact on the disk evolution (Fernández and

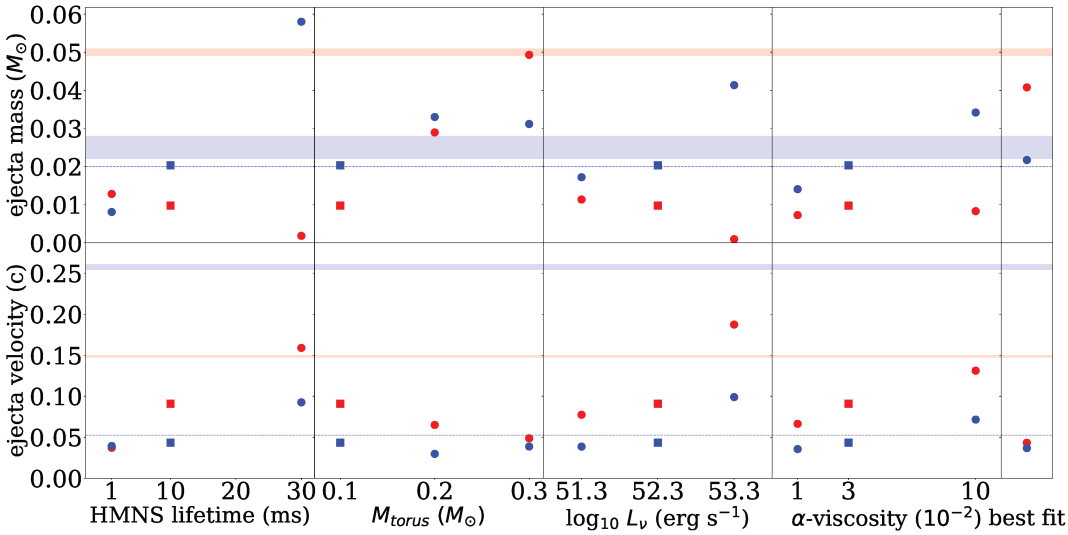

Figure 2.1: Ejected mass (top) and mass-averaged velocity (bottom) of the unbound disk outflow as a function of selected parameters: HMNS lifetime, initial torus mass, initial HMNS neutrino/antineutrino luminosity, and α-viscosity parameter. The rightmost panel shows our 'best fit' model. Red and blue symbols denote lanthanide-rich ($Y_e < 0.25$) and poor material, respectively, with squares denoting our 'base' model (Table 2.1). Data points have a fiducial uncertainty of 10% due to resolution. The horizontal red and blue bands correspond to the two-component fit of GW170817 by Villar et al. (2017), while the horizontal dotted blue line corresponds to the (average) disk outflow values used by Kawaguchi et al. (2018).

Metzger 2013; MF14).

2.2 Results

2.2.1 Overview of Disk Evolution

The qualitative evolution of the torus is independent of parameter choices, for details see MF14 and Lippuner et al. (2017). While the HMNS is present, accretion of the disk forms a high-density ($\sim 10^{12}$ g cm^{-3}) boundary layer around the HMNS. Due to intense neutrino and viscous heating, material is ejected from the boundary layer and from the edges of the disk on the local thermal time (~ 10 ms). Material escaping within ~ 20 deg of the polar axis

has $Y_e \sim 0.5$ due to strong irradiation, while on the equator the outflow has a Y_e closer to the initial disk value. The bulk of the disk remains neutron-rich ($Y_e \sim 0.2$) due the higher densities and shadowing of neutrino irradiation.

Upon collapse of the HMNS into a BH, the boundary layer accretes within ~ 0.1 ms, and a rarefaction wave is launched outward. The torus readjusts on the equatorial plane, evacuating the polar funnel. After a viscous time ($\sim 100 - 300\,\mathrm{ms}$), weak interactions freeze out and mass is ejected due to heating by viscosity and nuclear recombination. By this time the electron fraction of the outflow is higher than the initial disk value due to the lower degeneracy ($Y_e \sim 0.2 - 0.3$).

2.2.2 Parameter Sensitivity

Table 2.1 shows the mass and mass-averaged radial velocity of unbound disk ejecta for all models, as measured at a radius $r = 10^9\,\mathrm{cm}$. We use $Y_e = 0.25$ to divide the ejecta into lanthanide-poor ('blue') and lanthanide-rich ('red') material (e.g., Lippuner and Roberts 2015). Figure 2.1 illustrates the most sensitive parameter dependencies. While here we use the two-component fit of Villar et al. (2017) as a reference observational result, our general conclusions are independent of the specific (multi-component) kilonova fit used.

Our baseline model ejects an amount of mass with $Y_e > 0.25$ that approaches the observationally-inferred value, but there is insufficient lanthanide-rich mass ejected by a factor of 5. Also, the average velocity of the blue component is lower than that of the red ejecta, with the latter being $0.09c$ only.

The larger amount of blue relative to red ejecta for the default HMNS lifetime ($\sim 10\,\mathrm{ms}$) differs from that obtained by MF14, because the latter used a non-spinning BH after HMNS collapse. The red ejecta is produced in the initial thermal expansion of the disk on the side of the torus opposite to the HMNS, before weak interactions have time to significantly reprocess the disk composition, and therefore depends entirely on the initial condition chosen in

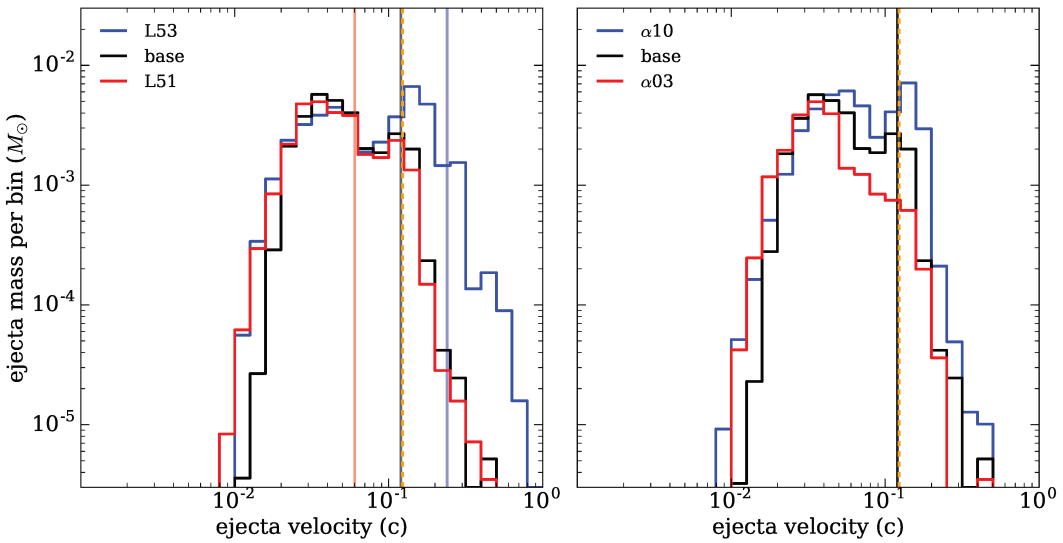

Figure 2.2: Mass histogram of unbound material ejected at $r = 10^9$ cm, as a function of velocity, for models that vary the magnitude of the initial HMNS luminosity (left) and the viscosity parameter (right), as labeled. The vertical solid lines show the asymptotic velocity for a pure neutrino driven wind (equation 2.1), and the vertical dashed line shows the maximum velocity achievable from alpha particle recombination energy alone (equation 2.2).

the baseline model ($Y_e = 0.1$). Model ye25 imposes $Y_e = 0.25$ initially in the disk, resulting in negligible red ejecta.

Increasing the HMNS lifetime, viscosity parameter, or initial HMNS luminosity results in the same trend: higher blue mass ejected, constant or decreasing red mass, and moderate increase in the outflow velocities. In all cases, the average velocity of the blue ejecta does not exceed $0.1c$, and the red ejecta exceeds $0.15c$ only when its mass is $\ll 0.01\,M_\odot$. The physics behind this trend is different in each case: longer HMNS lifetime results in longer neutrino irradiation and absence of mass/energy loss to the BH, higher viscosity parameter increases viscous heating (thereby increasing the entropy and thus equilibrum Y_e) and accelerates the disk evolution, while a higher HMNS luminosity increases the strength of neutrino heating and accelerates the rate of change of Y_e.

Increasing the torus mass increases the lanthanide-rich mass, in part due to

a larger thermal outflow that contains the most neutron-rich material, but also because the late-time viscous outflow becomes more neutron-rich. The blue mass peaks at $M_t = 0.2\,M_\odot$ and then decreases for higher tori masses. The average velocities of both components remain below $0.05c$.

Changes in the initial torus properties other than mass or composition produce minor quantitative changes, as illustrated by models rt60 and s10. Similarly, changes in the mass of the central object yield the same qualitative result. Increasing the HMNS radius increases the surface area of the star and decreases the density in the boundary layer, resulting in stronger torus irradiation and thus a higher electron fraction in the outflow. However, the total ejected mass is not significantly affected. We caution that these effects may be unique to our treatment of the HMNS as a hard boundary.

Finally, our best fit model involves increasing the torus mass and formation radius. The combination of these effects creates outflows with red and blue masses close to observational fits (allowing for an additional $0.01\,M_\odot$ supplement of red dynamical ejecta), but with lower average velocities for the blue component than required.

2.2.3 Physical Constraints on the Outflow Velocity

The initial thermal outflow is launched by a combination of viscous and neutrino heating. Viscous angular momentum transport enhances the outflow relative to a pure neutrino driven wind, by transporting material to shallower regions of the potential well, in addition to enhancing energy deposition (Lippuner et al., 2017).

Figure 2.2 illustrates the magnitude of this effect for models that vary the neutrino luminosity and viscosity parameter. The velocity distribution of the outflow is broad, and always exceeds the asymptotic velocity obtained in steady-state neutrino-driven wind models (Thompson et al., 2001; Metzger

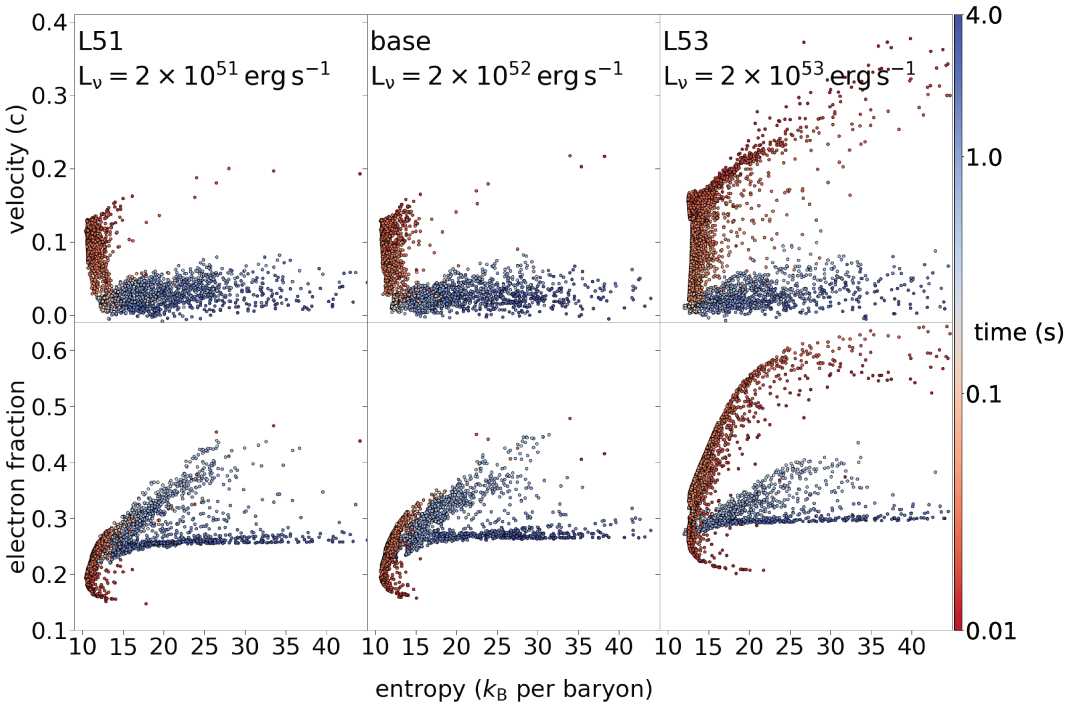

Figure 2.3: Properties of tracer particles ejected with positive energy, for models that vary the HMNS luminosity, as labeled, illustrating the different components of the disk outflow. The color of each particle corresponds to the time at which the temperature is $T = 5 \times 10^9\,\mathrm{K}$ for the last time before ejection. The velocity, electron fraction, and entropy shown are the values attained at this time.

et al., 2018)

$$v_\nu \approx 0.12c\left(\frac{L_\nu}{2\times 10^{52}}\right)^{0.3}. \tag{2.1}$$

The low-velocity portion of the distribution is ubiquitous to all models, arising from the late-time viscous/recombination-driven outflow which is launched once the disk has spread to larger radii. This component has an upper limit close to the maximum velocity that can be gained from nuclear recombination of alpha particles

$$v_{\rm rec} = \sqrt{2B_\alpha/m_\alpha} \approx 0.12c, \tag{2.2}$$

where B_α and m_α are nuclear binding energy and mass of an alpha particle (see, e.g., Fernández et al. 2019).

The different components of the outflow can be separated with tracer particles (Lippuner et al., 2017), as shown in Figure 2.3 for the models that vary the neutrino luminosity. The prompt ($t < 0.1\,$s) neutrino-driven wind appears as a tight correlation between the entropy and electron fraction of the particles. The importance of this component increases significantly with increasing neutrino luminosity, with the correlation extending to higher velocities and electron fractions. An intermediate component ($0.1 < t < 1\,$s) also shows a correlation between entropy and electron fraction extending up to $Y_e = 0.4$, but with a larger scatter than the prompt outflow and a lower velocity ($< 0.1c$). The late-time viscous/recombination-powered wind in the advective phase ($t > 1\,$s) has nearly constant average velocity ($\lesssim 0.05c$) and electron fraction ($\lesssim 0.3$), but with a wide range of entropies.

Out of these components, only the prompt viscously-enhanced neutrino-driven wind is able to significantly exceed $0.1c$. However, in our most extreme case (model L53), the ejected mass with speeds above $0.2c$ and $Y_e > 0.25$ is less than $3\times 10^{-3}\,M_\odot$.

We conclude that a combination of neutrino heating and viscous angular momentum transport in hydrodynamics is not able to account for the observed

components of the GW170817 when considering the HMNS disk outflow alone. This conclusion is not altered by our omission of full general relativistic effects, since the dynamics close to the BH horizon is not a key element for the generation of outflows while the HMNS is present, and our results are consistent with those of Fujibayashi et al. (2018), who include all relativistic effects.

2.2.4 Homologous Disk Ejecta

For reference, we provide fits to our disk ejecta once it has reached homologous expansion, as needed for radiative transfer models. We compute the evolution into this phase ($\sim 1000\,$s after merger) following the same method as in Kasen et al. (2015). Figure 2.4 shows the density and electron fraction profiles for the baseline model in this phase. For the ejecta density, we obtain acceptable fits with a broken power-law over a finite velocity range:

$$\rho/\rho_0 = \begin{cases} (v/v_0)^{-\eta_0} & v_0 < v < v_1 \\ (v_1/v_0)^{-\eta_0}\,(v/v_1)^{-\eta_1} & v_1 < v < v_2, \end{cases} \tag{2.3}$$

where ρ and v are the ejecta density and radial velocity, respectively. The velocity range $[v_0, v_2]$ is fixed by requiring that 90% of the energy is kinetic, and it is beyond the turbulent region ($r > 1.26 \times 10^6$ km). The remaining variables $(\rho_0, v_1, \eta_0, \eta_1)$ are fit parameters.

The electron fraction has a more complicated behavior, hence we do not attempt to fit it. Parameters for equation (2.3) and average electron fraction are given in Table 2.2.

2.3 Summary and Discussion

We have studied the long-term outflows from disks around HMNS remnants that collapse into BHs, using axisymmetric hydrodynamic simulations that include the dominant physical effects save for magnetic stresses. We find that for

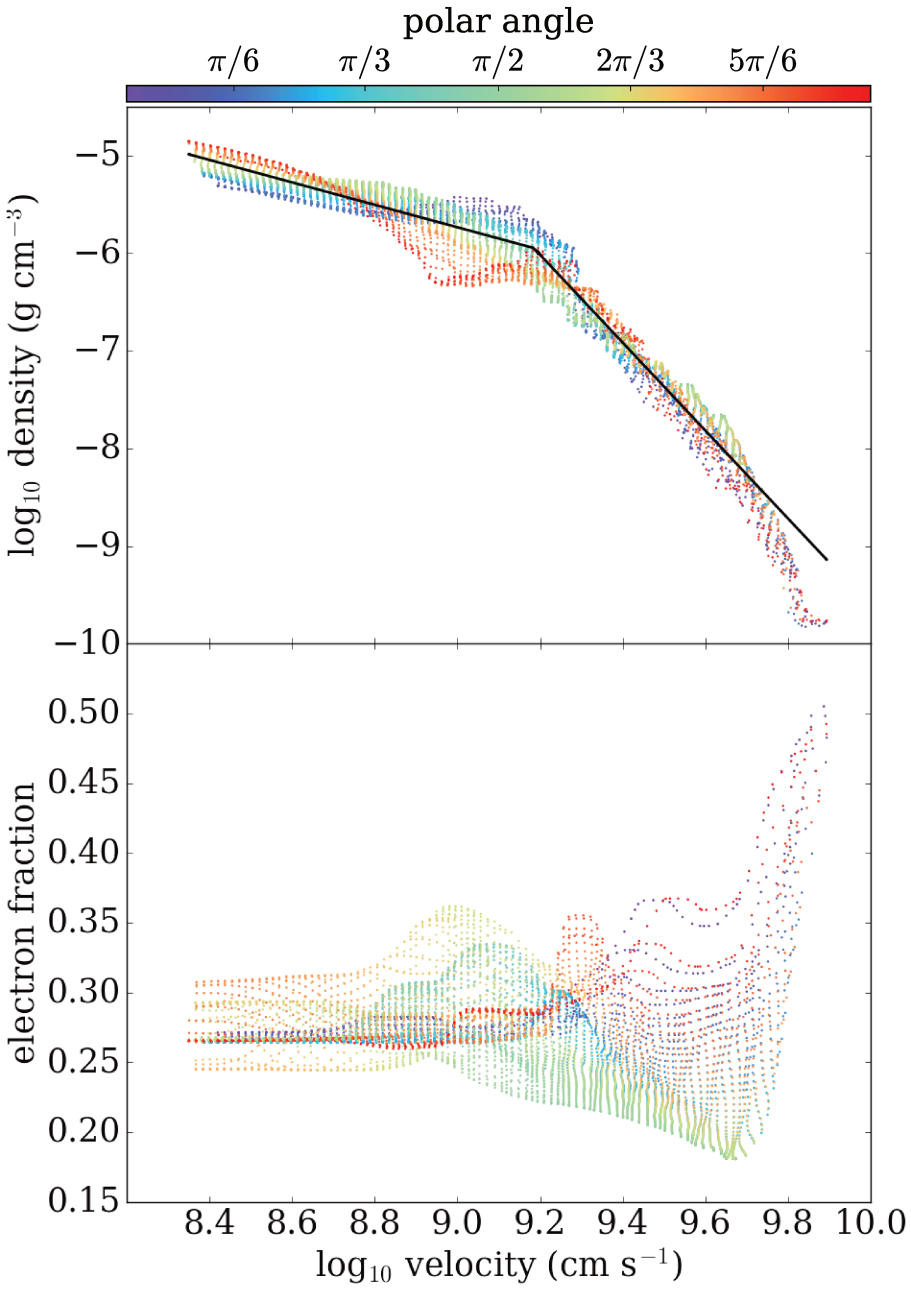

Figure 2.4: Ejecta in the homologous phase for the base model ($t = 1000$ s), shown as density (top) and electron fraction (bottom) as a function of radial velocity in each computational cell, colored by polar angle. The solid line shows a broken power-law fit to the density profile.

Model	$\rho_0/10^{-5}$ ($\mathrm{g\,cm^{-3}}$)	v_0/c (10^{-3})	v_1/c (10^{-2})	v_2/c (10^{-1})	η_0	η_1	$\bar{Y}_e$
base	1.024	7.479	5.101	2.604	1.150	4.503	0.264
a10	0.745	7.771	6.119	2.872	1.125	3.678	0.287
a03	4.485	6.955	3.827	2.371	1.788	4.858	0.260
t01	2.414	7.172	5.347	1.443	1.665	7.671	0.238
t30	0.585	7.739	5.337	3.146	0.875	2.946	0.354
M2.7	2.195	7.138	4.619	2.696	1.479	4.154	0.269
M2.6	2.430	7.109	6.632	2.459	1.741	5.276	0.257
L51	1.893	7.488	5.234	2.314	1.525	4.708	0.254
L53	1.667	7.535	4.728	4.349	1.512	3.252	0.354
mt03	6.673	6.828	4.586	2.263	1.404	5.266	0.233
mt02	3.714	6.822	3.461	2.501	0.996	4.376	0.242
rt60	3.551	6.868	5.747	2.251	1.818	5.589	0.242
rs30	2.543	7.214	4.126	2.019	1.445	5.197	0.233
s10	1.601	7.414	4.352	2.366	1.125	4.936	0.235
ye25	1.299	7.463	4.091	2.482	1.095	4.010	0.311
best	6.284	6.623	4.597	2.415	1.354	5.673	0.233

Table 2.2: Parameters of the broken power-law fit to the density in homology (equation 2.3). For reference, we also provide the mass-averaged electron fraction of the outflow.

plausible parameters compatible with GW170817, hydrodynamic disk outflow models that employ shear viscosity to transport angular momentum cannot achieve mass-averaged velocities compatible with the blue kilonova as inferred from multi-component kilonova fits. While the ejected mass can in principle be brought closer to the inferred values by a suitable parameter choice, the same cannot be achieved for the velocities of both components.

Kawaguchi et al. (2018) find that radiative transfer simulations that include reprocessing of photons from the disk outflow by the dynamical ejecta do not require a disk wind expanding faster than $0.1c$ to explain the GW170817 kilonova. Here the dynamical ejecta provides a velocity boost to these blue photons, and eliminates the need for high ejecta masses, bringing it into agreement with current predictions from numerical relativity simulations. Our disk outflow models are fully compatible with their results (c.f. Figure 2.1). Establishing whether this is the correct resolution to the wind velocity problem requires further work.

Alternatively, state-of-the-art numerical relativity simulations predict too little dynamical ejecta to reconcile the large masses moving at $0.25c$. Enhancements in this prompt ejecta can be obtained for example by viscous effects, either by ejecting material directly from the HMNS at early times (Shibata et al., 2017b), or by thermally boosting the dynamical ejecta (Radice et al., 2018). The robustness of these effects remains to be further explored.

The only remaining way to significantly boost the disk velocities are magnetic stresses. Initial three-dimensional GRMHD models of BH remnant disks show that this can easily be achieved (Siegel and Metzger, 2018; Fernández et al., 2019). The conjecture is further supported by early-phase simulations of magnetized, differentially rotating HMNS remnants (e.g., Kiuchi et al. 2012; Siegel et al. 2014). Including the effects of magnetic fields is the most straightforward way to improve our simulations.

Chapter 3

Hydrodynamics on a Three Dimensional Spherical Mesh

Due to the uncertainty in viscous parameterization of magnetic fields, the next logical step is to construct an equilibrium torus using magnetohydrodynamics (MHD), requiring 3 dimensions to avoid suppressing the MRI (e.g., Igumenshchev and Abramowicz 1999; Stone et al. 1999). With this advancement we can also input an equilibrium HMNS, eliminating uncertainties over the use of a reflecting boundary condition at the surface of the star.

More recent results using MHD show promise in recreating the kilonova, but more research is required. Many of these results suffer the same flaws as the hydrodynamic (HD) simulations: Some are not directly applicable to GW170817 and do not use full neutrino transport (Siegel and Metzger, 2018; Ciolfi et al., 2019; Fernández et al., 2019), or do not run for sufficiently long and use only a BH (Miller et al., 2019). Although in principle these simulations can be run in any coordinate system, the most advantageous setup involves a spherical grid. The sphericity of the star is preserved, which allows for easy implementation of periodic boundaries. In addition, this allows for natural conservation of angular momentum as less numerical diffusion happens through a ϕ-border of a spherical cell, as there is minimal flow diagonal to the grid cells.

Since the majority of important effects occur with ϕ-symmetry (e.g., neutrino emission, MRI, recombination, etc...), we can reduce the resolution along the ϕ-axis with minimal loss of accuracy. In the radial direction, a non-uniform logarithmic grid can also be used to increase the range of the simulation without incurring large computational costs. This line of reasoning is broadly applicable to many astrophysical systems, like CCSN.

As a stepping stone to reach full MHD, we implement the capability to perform 3D hydrodynamical simulations into the publicly available astrophysical code `FLASH4.5` (Dubey et al., 2009). The public version currently supports the divergence-free evolution of magnetic fields in 3D Cartesian coordinates, but not 3D spherical coordinates.

We modify the default dimensionally unsplit solver (Lee, 2013), which solves the HD Euler equations in each direction simultaneously by including contributions at each face from transverse and diagonal fluxes. This has a straightforward expansion to MHD (see §4), and the testing and implementation of pure hydro fits well into the timeline to complete this MSc thesis.

3.1 Governing Equations of Hydrodynamics

The conservation equations are those of mass, momentum and energy. These can be written as

$$\frac{\partial \rho}{\partial t} + \nabla \cdot [\rho \mathbf{v}] = 0, \tag{3.1}$$

$$\frac{\partial (\rho \mathbf{v})}{\partial t} + \nabla \cdot [\rho (\mathbf{v} \otimes \mathbf{v})] + \nabla P = 0, \tag{3.2}$$

$$\frac{\partial (\rho E)}{\partial t} + \nabla \cdot [\mathbf{v}(\rho E + P)] = 0, \tag{3.3}$$

where ρ is the density, $\mathbf{v}$ is the vector velocity, E is the total energy, and P is defined as the total gas pressure. The HD equations can written as a set of

conserved variables, $\mathbf{U}$, associated fluxes, $\mathcal{F}$, and source terms, $\mathbf{S}$,

$$\frac{\partial \mathbf{U}}{\partial t} + \nabla \cdot \mathcal{F} = \mathbf{S}. \tag{3.4}$$

To make the reduction or addition of dimensions easier, the associated fluxes are usually expanded as (in spherical coordinates)

$$\frac{\partial \mathbf{U}}{\partial t} + \frac{1}{r^2}\frac{\partial (r^2 \mathbf{F})}{\partial r} + \frac{1}{r \sin\theta}\frac{\partial (\sin\theta \mathbf{G})}{\partial \theta} + \frac{1}{r \sin\theta}\frac{\partial \mathbf{H}}{\partial \phi} = \mathbf{S}, \tag{3.5}$$

where the additional source terms arise from the finite curvature of spherical geometry. The conserved variables and fluxes in the r, θ, and ϕ directions, $\mathbf{U}, \mathbf{F}, \mathbf{G}$, and $\mathbf{H}$, respectively, are defined as

$$\mathbf{U} = \left(\rho, \rho v_r, \rho v_\theta, \rho v_\phi, \rho E\right)^T, \tag{3.6}$$

$$\mathbf{F} = \begin{pmatrix} \rho v_r \\ \rho v_r^2 + P \\ \rho v_r v_\theta \\ \rho v_r v_\phi \\ v_r(\rho E + P) \end{pmatrix}, \mathbf{G} = \begin{pmatrix} \rho v_\theta \\ \rho v_\theta v_r \\ \rho v_\theta^2 + P \\ \rho v_\theta v_\phi \\ v_\theta(\rho E + P) \end{pmatrix}, \mathbf{H} = \begin{pmatrix} \rho v_\phi \\ \rho v_\phi v_r \\ \rho v_\theta v_\phi \\ \rho v_\phi^2 + P \\ v_\phi(\rho E + P) \end{pmatrix}. \tag{3.7}$$

In conservative mesh based codes such as the finite volume method that `FLASH` employs, the conserved variables are evolved by discretizing (3.5) in both time and space. This means that we evolve each variable by taking a volume average over the cell, and then advance the volume averaged variable using the corresponding volume averaged incoming and outgoing fluxes at the faces. Using the notation $\{i, j, k\} + 1/2$ to represent variables at the corresponding

faces, and n to step in time, this can be written concisely as

$$\begin{aligned}\mathbf{U}^{n+1} = \mathbf{U}^{n} - \frac{\Delta t}{V}\Bigg(& (A_{i-1/2}\mathbf{F}_{i-1/2} - A_{i+1/2}\mathbf{F}_{i+1/2}) \\ & - (A_{j-1/2}\mathbf{G}_{j-1/2} - A_{j+1/2}\mathbf{G}_{j+1/2}) \\ & - (A_{k-1/2}\mathbf{H}_{k-1/2} - A_{k+1/2}\mathbf{H}_{k+1/2})\Bigg) + \Delta t\langle \mathbf{S} \rangle, \end{aligned} \tag{3.8}$$

where $A_{i,j,k}$ is the area of the face perpendicular to the corresponding direction, and V is volume of the cell. We have used Gauss's Law,

$$\iiint_V \nabla \cdot \mathbf{F} \mathrm{d}V = \oiint_A \mathbf{F} \cdot \mathrm{d}\mathbf{A}, \tag{3.9}$$

to write the volume averaged fluxes as face-centered fluxes. To get to this point we need a few key ingredients. The first is initial conditions, which will vary by problem. Second, we need fluxes at each face, discussed in §3.3, and the third is the volume averaged geometric source terms, which are discussed below.

3.2 Geometric Source Terms

The geometric source terms arise from taking covariant derivatives of second rank tensors, referred to as a tensor divergence. In spherical coordinates, this can be written for a generic tensor, T, as (see Appendix §A, or Mignone et al. 2005 for a separate derivation)

$$\nabla \cdot T = \begin{pmatrix} \nabla_r T \\ \nabla_\theta T \\ \nabla_\phi T \end{pmatrix}, \tag{3.10}$$

where we can define the divergences in each individual direction, starting in the radial direction:

$$\nabla_r T = \left(\frac{1}{r^2} \frac{\partial (r^2 T^{rr})}{\partial r} + \frac{1}{r \sin\theta} \frac{\partial (\sin\theta T^{\theta r})}{\partial \theta} + \frac{1}{r \sin\theta} \frac{\partial T^{\phi r}}{\partial \phi} - \frac{T^{\theta\theta} + T^{\phi\phi}}{r} \right), \tag{3.11}$$

in the polar,

$$\nabla_\theta T = \left(\frac{1}{r^2} \frac{\partial (r^2 T^{r\theta})}{\partial r} + \frac{1}{r \sin\theta} \frac{\partial (\sin\theta T^{\theta\theta})}{\partial \theta} + \frac{1}{r \sin\theta} \frac{\partial T^{\phi\theta}}{\partial \phi} + \frac{T^{\theta r}}{r} - \frac{T^{\phi\phi}}{r} \cot\theta \right), \tag{3.12}$$

and in the azimuthal,

$$\nabla_\phi T = \left(\frac{1}{r^2} \frac{\partial (r^2 T^{r\phi})}{\partial r} + \frac{1}{r \sin\theta} \frac{\partial (\sin\theta T^{\theta\phi})}{\partial \theta} + \frac{1}{r \sin\theta} \frac{\partial T^{\phi\phi}}{\partial \phi} + \frac{T^{\phi r}}{r} + \frac{T^{\phi\theta}}{r} \cot\theta \right). \tag{3.13}$$

In both the mass and energy conservation equations we only take the first rank tensor (vector) divergence, and therefore no additional source terms are needed to satisfy Gauss's Law. We turn our attention then to the momentum equation, which can be explicitly written as a second rank tensor (dyad) by using the outer product

$$\frac{\partial}{\partial t} \begin{pmatrix} \rho v_r \\ \rho v_\theta \\ \rho v_\phi \end{pmatrix} + \nabla \cdot \begin{pmatrix} \rho v_r^2 & \rho v_r v_\theta & \rho v_r v_\phi \\ \rho v_r v_\theta & \rho v_\theta^2 & \rho v_\theta v_\phi \\ \rho v_r v_\phi & \rho v_\theta v_\phi & \rho v_\phi^2 \end{pmatrix} + \nabla P = 0. \tag{3.14}$$

Explicitly applying the divergences (3.11)-(3.13) to the dyad yields the three momentum equations in the r, θ, ϕ directions

$$\frac{\partial(\rho v_r)}{\partial t} + \frac{1}{r^2}\frac{\partial(r^2[\rho v_r^2])}{\partial r} + \frac{1}{r\sin\theta}\frac{\partial(\sin\theta[\rho v_\theta v_r])}{\partial\theta} + \frac{1}{r\sin\theta}\frac{\partial(\rho v_\phi v_r)}{\partial\phi} + \frac{\partial P}{\partial r} = \frac{\rho(v_\theta^2 + v_\phi^2)}{r}, \tag{3.15}$$

$$\frac{\partial(\rho v_\theta)}{\partial t} + \frac{1}{r^2}\frac{\partial(r^2[\rho v_r v_\theta])}{\partial r} + \frac{1}{r\sin\theta}\frac{\partial(\sin\theta[\rho v_\theta^2])}{\partial\theta} + \frac{1}{r\sin\theta}\frac{\partial(\rho v_\phi v_\theta)}{\partial\phi} + \frac{1}{r}\frac{\partial P}{\partial\theta} = -\frac{\rho v_r v_\theta}{r} + \frac{\cot\theta(\rho v_\phi^2)}{r}, \tag{3.16}$$

$$\frac{\partial(\rho v_\phi)}{\partial t} + \frac{1}{r^2}\frac{\partial(r^2[\rho v_r v_\phi])}{\partial r} + \frac{1}{r\sin\theta}\frac{\partial(\sin\theta[\rho v_\phi v_\theta])}{\partial\theta} + \frac{1}{r\sin\theta}\frac{\partial(\rho v_\phi^2)}{\partial\phi} + \frac{1}{r\sin\theta}\frac{\partial P}{\partial\phi} = -\frac{\rho v_r v_\phi}{r} - \frac{\cot\theta(\rho v_\phi v_\theta)}{r}. \tag{3.17}$$

The spatial derivatives on the left-hand side can now be treated as vector divergences using Gauss's Law, however they require the addition of the source terms on the right hand side. Finally, for use in (3.8) these source terms must be volume averaged,

$$\frac{1}{V}\iiint_V \mathbf{S}(r,\theta)\mathrm{d}V. \tag{3.18}$$

For example, in the r momentum flux equation, we have that

$$S_{\rho v_r}(r) = \frac{\rho v_\theta^2}{r}, \tag{3.19}$$

so our integral over the cell becomes

$$\frac{1}{V}\iiint_V S_{\rho v_r}(r)\mathrm{d}V = -\frac{3}{\Delta\phi\Delta\cos\theta\Delta r^3}\int_{\phi_{k-1/2}}^{\phi_{k+1/2}}\int_{\theta_{j-1/2}}^{\theta_{j+1/2}}\int_{r_{i-1/2}}^{r_{i+1/2}}\frac{\rho(v_\theta^2+v_\phi^2)}{r}r^2\sin\theta\mathrm{d}r\mathrm{d}\theta\mathrm{d}\phi \approx \frac{3}{2}\frac{\Delta r^2}{\Delta r^3}\Big(\langle\rho\rangle\langle v_\theta\rangle^2 + \langle\rho\rangle\langle v_\phi\rangle^2\Big), \tag{3.20}$$

where we define the finite differences

$$\Delta r^2 = r_{i+1/2}^2 - r_{i-1/2}^2, \tag{3.21}$$

$$\Delta r^3 = r_{i+1/2}^3 - r_{i-1/2}^3, \tag{3.22}$$

$$\Delta \cos\theta = \cos\theta_{i+1/2} - \cos\theta_{i-1/2}. \tag{3.23}$$

In the final step, the primitive variables are taken to be the volume averages to match the other variables in the conservative update. In both the $\hat{\phi}$ and $\hat{\theta}$ momentum fluxes we must also integrate over θ,

$$\begin{aligned}\frac{1}{V}\iiint_V S_{\rho v_\theta}(r,\theta)\mathrm{d}V = \\ -\frac{3}{\Delta\phi\Delta\cos\theta\Delta r^3}\int_{\phi_{k-1/2}}^{\phi_{k+1/2}}\int_{\theta_{j-1/2}}^{\theta_{j+1/2}}\int_{r_{i-1/2}}^{r_{i+1/2}}\left(\frac{-\rho v_r v_\theta}{r}+\frac{(\rho v_\phi^2)\cot\theta}{r}\right)r^2\sin\theta\mathrm{d}r\mathrm{d}\theta\mathrm{d}\phi \\ \approx -\frac{3\Delta r^2}{2\Delta r^3}\langle\rho\rangle\langle v_r\rangle\langle v_\theta\rangle - \frac{3\Delta r^2}{2\Delta r^3}\frac{\Delta\sin\theta}{\Delta\cos\theta}\langle\rho\rangle\langle v_\phi\rangle^2.\end{aligned} \tag{3.24}$$

In the exact same way, we find that

$$\frac{1}{V}\iiint_V S_{\rho v_\phi}(r,\theta)\mathrm{d}V \approx -\frac{3\Delta r^2}{2\Delta r^3}\langle\rho\rangle\langle v_r\rangle\langle v_\phi\rangle + \frac{3\Delta r^2}{2\Delta r^3}\frac{\Delta\sin\theta}{\Delta\cos\theta}\langle\rho\rangle\langle v_\phi\rangle\langle v_\theta\rangle. \tag{3.25}$$

Since there are common terms to each of the volume integrals, we save on computation and implement this numerically by defining the geometric integration terms

$$dy_{\mathrm{sph}} = -\frac{\Delta\sin\theta}{\Delta\cos\theta} = \frac{\sin\theta_{j+1/2}-\sin\theta_{j-1/2}}{\cos\theta_{j-1/2}-\cos\theta_{i+1/2}}, \tag{3.26}$$

$$\begin{aligned}dx_{\mathrm{sph}} &= \frac{3\Delta r^2}{2\Delta r^3} = \frac{3(r_{i-1/2}+r_{i+1/2})(r_{i+1/2}-r_{i-1/2})}{2(r_{i+1/2}-r_{i-1/2})(r_{i-1/2}^2+r_{i-1/2}r_{i+1/2}+r_{i+1/2}^2)} \\ &= \frac{3r}{(r_{i-1/2}^2+r_{i-1/2}r_{i+1/2}+r_{i+1/2}^2)}.\end{aligned} \tag{3.27}$$

Doing this reduces our source term equations to

$$\langle S_{\rho v_r} \rangle = dx_{\text{sph}} \bigg(\langle \rho \rangle \langle v_\theta \rangle^2 + \langle \rho \rangle \langle v_\phi \rangle^2 \bigg), \tag{3.28}$$

$$\langle S_{\rho v_\theta} \rangle = dx_{\text{sph}} \bigg(- \langle \rho \rangle \langle v_r \rangle \langle v_\theta \rangle + dy_{\text{sph}} \langle \rho \rangle \langle v_\phi \rangle^2 \bigg), \tag{3.29}$$

$$\langle S_{\rho v_\phi} \rangle = dx_{\text{sph}} \bigg(- \langle \rho \rangle \langle v_r \rangle \langle v_\phi \rangle - dy_{\text{sph}} \langle \rho \rangle \langle v_\phi \rangle \langle v_\theta \rangle \bigg). \tag{3.30}$$

3.3 Fluxes and Primitive Variables

Now that we have the source terms, we must compute the fluxes in (3.5) and (3.7). This is done in the reconstruction step, using the so-called primitive variables, given in the vector $\mathbf{V}$ (not to be confused with the velocities, $\mathbf{v}$), and their corresponding evolution equations

$$\mathbf{V} = (\rho, v_r, v_\theta, v_\phi, P)^T, \tag{3.31}$$

$$\frac{\partial \rho}{\partial t} + \mathbf{v} \cdot \nabla \rho + \rho (\nabla \cdot \mathbf{v}) = 0, \tag{3.32}$$

$$\frac{\partial \mathbf{v}}{\partial t} + (\mathbf{v} \cdot \nabla) \cdot \mathbf{v} + \frac{1}{\rho} \nabla P = 0, \tag{3.33}$$

$$\frac{\partial P}{\partial t} + \mathbf{v} \cdot \nabla P + \gamma P (\nabla \cdot \mathbf{v}) = 0. \tag{3.34}$$

The primitive mass (3.32) and momentum equations (3.33) result from simple expansion of derivatives in the conservative formulations. The primitive pressure equation comes from the first law of thermodynamics, where for a general EOS, $P = P(\rho, s)$, and therefore (Following Zingale 2019, Chapter 7)

$$\frac{\partial P}{\partial t} = \frac{\partial P}{\partial \rho}\bigg|_s \frac{\partial \rho}{\partial t} + \frac{\partial P}{\partial s}\bigg|_\rho \frac{\partial s}{\partial t}. \tag{3.35}$$

When the hydrodynamics are evolved separately from the source terms that modify the entropy, we can assume adiabatic expansion provides the only changes in pressure. This implies there are no local entropy sources, and the

final term goes to zero. Replacing $\partial\rho/\partial t$ with equation (3.32) yields

$$\frac{\partial P}{\partial t} + \frac{\partial P}{\partial \rho}(\mathbf{v} \cdot \nabla\rho + \rho\nabla \cdot \mathbf{v}) = 0. \tag{3.36}$$

We can use the adiabatic index

$$\gamma = \left(\frac{\mathrm{d}\log P}{\mathrm{d}\log\rho}\right)\bigg|_s, \tag{3.37}$$

and the fact that

$$\frac{\partial P}{\partial \rho}(\mathbf{v} \cdot \nabla\rho) = \mathbf{v} \cdot \nabla P, \tag{3.38}$$

to arrive at the final result

$$\frac{\partial P}{\partial t} + \mathbf{v} \cdot \nabla P + \gamma P(\nabla \cdot \mathbf{v}) = 0. \tag{3.39}$$

The advantage to working with primitive variables is that this system and their partial derivatives can be written in a quasi-linear fashion, taking the form

$$\frac{\partial \mathbf{V}}{\partial t} + \mathbf{A}_r\frac{\partial \mathbf{V}}{\partial r} + \mathbf{A}_\theta\frac{1}{r}\frac{\partial \mathbf{V}}{\partial \theta} + \mathbf{A}_\phi\frac{1}{r\sin\theta}\frac{\partial \mathbf{V}}{\partial \phi} = \mathbf{S}, \tag{3.40}$$

where the matrices A_r, A_θ, A_ϕ can be written as (see Lee and Deane 2009 for a full derivation)

$$\mathbf{A}_r = \begin{pmatrix} v_r & \rho & 0 & 0 & 0 \\ 0 & v_r & 0 & 0 & 1/\rho \\ 0 & 0 & v_r & 0 & 0 \\ 0 & 0 & 0 & v_r & 0 \\ 0 & \gamma P & 0 & 0 & v_r \end{pmatrix}, \tag{3.41}$$

$$\mathbf{A}_\theta = \begin{pmatrix} v_\theta & 0 & \rho & 0 & 0 \\ 0 & v_\theta & 0 & 0 & 0 \\ 0 & 0 & v_\theta & 0 & 1/\rho \\ 0 & 0 & 0 & v_\theta & 0 \\ 0 & 0 & \gamma P & 0 & v_\theta \end{pmatrix}, \tag{3.42}$$

and

$$\mathbf{A}_\phi = \begin{pmatrix} v_\phi & 0 & 0 & \rho & 0 \\ 0 & v_\phi & 0 & 0 & 0 \\ 0 & 0 & v_\phi & 0 & 0 \\ 0 & 0 & 0 & v_\phi & 1/\rho \\ 0 & 0 & 0 & \gamma P & v_\phi \end{pmatrix}. \tag{3.43}$$

Alternatively, this can be thought of as an explicit expansion of all the partial derivatives in the conservation equations. This is the method that we will use to find the corresponding source terms in the evolution of primitive variables, referred to as the reconstruction step. Once written in this form, the cell-centered values can be interpolated to the faces by fitting polynomials. In `FLASH`, the default extrapolation is a piecewise linear MUSCL-Hancock method (PLM, Toro, 2013, Chapter 13.4), which can be thought of as simply a Taylor expansion of a cell-centered variable to each face, and then a Taylor expansion in time to half a timestep. The time centering is needed for the conservative update, where we achieve second order accuracy by centering the fluxes used for the update in time. We show an example of an expansion to the r faces (see also Figure 3.1), but an equivalent procedure is followed for both θ and ϕ,

$$\mathbf{V}^{n+1/2}_{i\pm1/2,j,k} = \mathbf{V}^{n}_{i,j,k} \pm \frac{\Delta r}{2}\frac{\partial \mathbf{V}}{\partial r} + \frac{\Delta t}{2}\frac{\partial \mathbf{V}}{\partial t} + \mathcal{O}([\Delta r]^2, [\Delta t]^2). \tag{3.44}$$

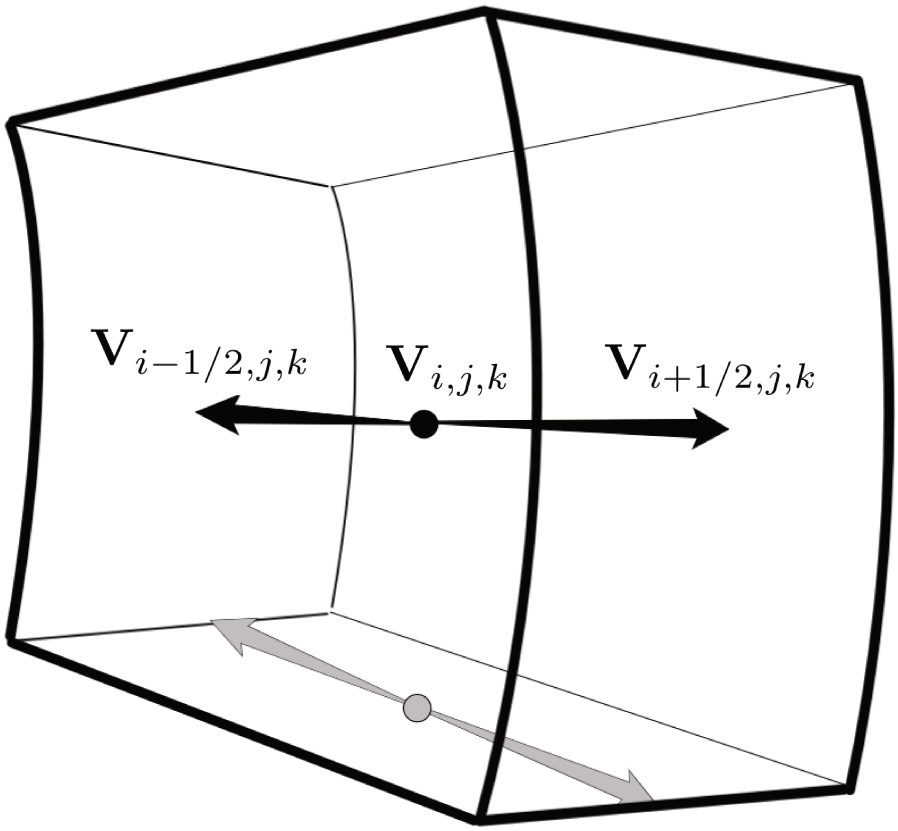

Figure 3.1: Example of spatially reconstructing a cell-centered primitive variable to the cell-centered face of a spherical cell, in the radial direction. A similar process is followed for the polar and azimuthal reconstructions (see text for details).

We can eliminate the temporal derivative by replacing it with the quasi-linear system, (3.40), and then eliminate the spatial derivative by approximating with a finite difference,

$$\begin{aligned}\mathbf{V}^{n+1/2}_{i\pm1/2,j,k} &= \mathbf{V}^{n}_{i,j,k} \pm \frac{\Delta r}{2}\frac{\partial \mathbf{V}}{\partial r} + \frac{\Delta t}{2}\left(A_r\frac{\partial \mathbf{V}}{\partial r} + \frac{A_\theta}{r\sin\theta}\frac{\partial \mathbf{V}}{\partial \theta} + \frac{A_\phi}{r\sin\theta}\frac{\partial \mathbf{V}}{\partial \phi} - \mathbf{S}\right) \\ &= \mathbf{V}^{n}_{i,j,k} + \frac{1}{2}\left(\pm\mathbf{I} - \frac{\Delta t}{\Delta r}A_r\right)\Delta\mathbf{V} + \frac{\Delta t}{2}\left(\frac{A_\theta}{r}\frac{\Delta \mathbf{V}}{\Delta\theta} + \frac{A_\phi}{r\sin\theta}\frac{\Delta \mathbf{V}}{\Delta\phi} - \mathbf{S}\right).\end{aligned} \tag{3.45}$$

This accounts for the parallel fluxes in the first term, and the transverse fluxes and geometry in the second. However, in 3D we also must account for *diagonal* fluxes between cells, which happen when the velocities in each r, θ, ϕ direction are close to equal. To do this, the process is much the same except that the primitive variables are expanded to $n+1/3$ and $i\pm1/3$. Luckily for our spherical implementation, this does not change the treatment of source terms. A similar process is followed for expansions in j and k. The expanded primitive variables at the face are then used to calculate the face-centered, time-centered fluxes utilized by the Riemann solver. However, we still need the primitive source terms to perform the expansion. We find the source terms by expanding the primitive equations, yielding for mass conservation:

$$\begin{aligned}\frac{\partial\rho}{\partial t} + v_r\frac{\partial\rho}{\partial r} + \frac{v_\theta}{r}\frac{\partial\rho}{\partial\theta} + \frac{v_\phi}{r\sin\theta}\frac{\partial\rho}{\partial\phi} + \rho\frac{\partial v_r}{\partial r} + \frac{\rho}{r}\frac{\partial v_\theta}{\partial\theta} + \frac{\rho}{r\sin\theta}\frac{\partial v_\phi}{\partial\phi} \\ = -\rho\left(\frac{2v_r + v_\theta\cot\theta}{r}\right).\end{aligned} \tag{3.46}$$

By examination, we can see that the pressure equation is almost exactly the same as (3.46), except instead of density, we have a γP or a P attached to our divergence and gradient, respectively. Using the adiabatic sound speed

relation, $c_s^2\rho = \gamma P$, we can rewrite (3.34) as

$$\frac{\partial P}{\partial t} + v_r\frac{\partial P}{\partial r} + \frac{v_\theta}{r}\frac{\partial P}{\partial \theta} + \frac{v_\phi}{r\sin\theta}\frac{\partial P}{\partial \phi} + \gamma P\frac{\partial v_r}{\partial r} + \frac{\gamma P}{r}\frac{\partial v_\theta}{\partial \theta} + \frac{\gamma P}{r\sin\theta}\frac{\partial v_\phi}{\partial \phi} = -c_s^2\rho\left(\frac{2v_r + v_\theta\cot\theta}{r}\right), \quad (3.47)$$

therefore ending up with the sound speed squared multiplied by our original density geometric factor. The primitive energy variable equation can be used to optionally evolve the internal energy separately in `FLASH`. It comes from expanding the conservative energy equation and removing terms using mass conservation. Expanding and dividing by energy, E, we find

$$\frac{\partial E}{\partial t} + \frac{P}{\rho}\left(\frac{\partial v_r}{\partial r} + \frac{1}{r}\frac{\partial v_\theta}{\partial \theta} + \frac{1}{r\sin\theta}\frac{\partial v_\phi}{\partial \phi}\right) = -\frac{h}{\rho}\rho\left(\frac{2v_r + v_\theta\cot\theta}{r}\right), \quad (3.48)$$

which is just the enthalpy ($h = E + P/\rho$) divided by the density, multiplied by our original density geometric factor. Next, we work out the momentum conservation equations, which we simplify using the mass conservation equation. Since the mass conservation equation simply subtracts one factor of

$$\rho\left(\frac{2v_r + v_\theta\cot\theta}{r}\right), \quad (3.49)$$

and then expanding the derivatives explicitly adds one, the net effect on the source terms is simply a division by ρ to get

$$\left(\frac{\partial v_r}{\partial t} + v_r\frac{\partial v_r}{\partial r} + \frac{v_\theta}{r}\frac{\partial v_r}{\partial \theta} + \frac{v_\phi}{r\sin\theta}\frac{\partial v_r}{\partial \phi}\right) + \frac{1}{\rho}\frac{\partial P}{\partial r} = \left(\frac{v_\theta^2 + v_\phi^2}{r}\right), \quad (3.50)$$

$$\left(\frac{\partial v_\theta}{\partial t} + v_r\frac{\partial v_\theta}{\partial r} + \frac{v_\theta}{r}\frac{\partial v_\theta}{\partial \theta} + \frac{v_\phi}{r\sin\theta}\frac{\partial v_\theta}{\partial \phi}\right) + \frac{1}{\rho r}\frac{\partial P}{\partial \theta} = \left(\frac{v_\phi^2\cot\theta - v_\theta v_r}{r}\right), \quad (3.51)$$

$$\left(\frac{\partial v_\phi}{\partial t} + v_r\frac{\partial v_\phi}{\partial r} + \frac{v_\theta}{r}\frac{\partial v_\phi}{\partial \theta} + \frac{v_\phi}{r\sin\theta}\frac{\partial v_\phi}{\partial \phi}\right) + \frac{1}{\rho r\sin\theta}\frac{\partial P}{\partial \phi} = -\left(\frac{v_\phi v_\theta\cot\theta + v_\phi v_r}{r}\right). \quad (3.52)$$

The terms on the right hand side are added as the geometric source terms during the reconstruction phase.

3.4 Evolution Timestep

In order to be physical, and therefore a numerically stable explicit method, the code must resolve the fastest moving wave in each cell. This sets the timestep for a given cell, and `FLASH` is designed to take the minimum timestep in the domain as the global timestep, to avoid synchronicity errors. This is often formally stated as the Courant-Friedrichs-Lewy (CFL) condition (e.g., Toro 2013; Zingale 2019), which states that in each direction

$$\frac{\max(c_s - v, c_s + v)\Delta t}{\Delta \ell} \leq \mathcal{C}, \tag{3.53}$$

where ℓ must have unit length and $\mathcal{C} \leq 1$. We define λ as the maximum wavespeed that we need to resolve,

$$\lambda_{\{i,j,k\}} = \max(c_s - v_{\{i,j,k\}}, c_s + v_{\{i,j,k\}}). \tag{3.54}$$

For spherical coordinates, we can explicitly write the CFL condition for each cell as

$$\Delta t \left(\frac{\lambda_r}{\Delta r}, \frac{\lambda_\theta}{r\Delta\theta}, \frac{\lambda_\phi}{r\sin\theta\Delta\phi} \right) \leq \mathcal{C}. \tag{3.55}$$

The important thing to note here is that our timestep is most restricted at small r and $\sin\theta$, corresponding to the inner radial, polar boundaries of the simulation.

Chapter 4

Implementation in FLASH4.5

FLASH is a highly adaptable mesh based code (Fryxell et al., 2000; Dubey et al., 2009), and we choose to implement full 3D hydrodynamics in it because the code is segmented into separate units, or modules. This makes it so that the modified hydrodynamics module is isolated from the other inner workings of the code (e.g., Grid, Gravity, EOS), and can be easily reused in other setups that would also benefit from spherical geometry (e.g., CCSN, mergers). We illustrate this in Figure 4.1, which shows the hierarchical organization of FLASH. Second, there is a straightforward expansion from unsplit hydrodynamics to unsplit magnetohydrodynamics, which will be part of future work in creating a magnetized torus. Third, hydrodynamics already functions in Cartesian, 1D spherical, and 2D Cylindrical (Tzeferacos et al., 2012), meaning that the framework for many of the modifications is already present (e.g., memory allocation for source terms, line/area/volume elements), but the specifics are not yet implemented. Finally, FLASH is capable of supporting adaptive mesh refinement (AMR), which provides a method to lift the restriction on the global timestep from the ϕ cells at small radii as discussed in equation (3.55).

In the hydrodynamics unit (see Figure 4.2), three major files must be modified. The reconstruction of source terms occurs in `hy_uhd_getRiemannState`, which carries out the Taylor expansion given in equation (3.45). It is here that

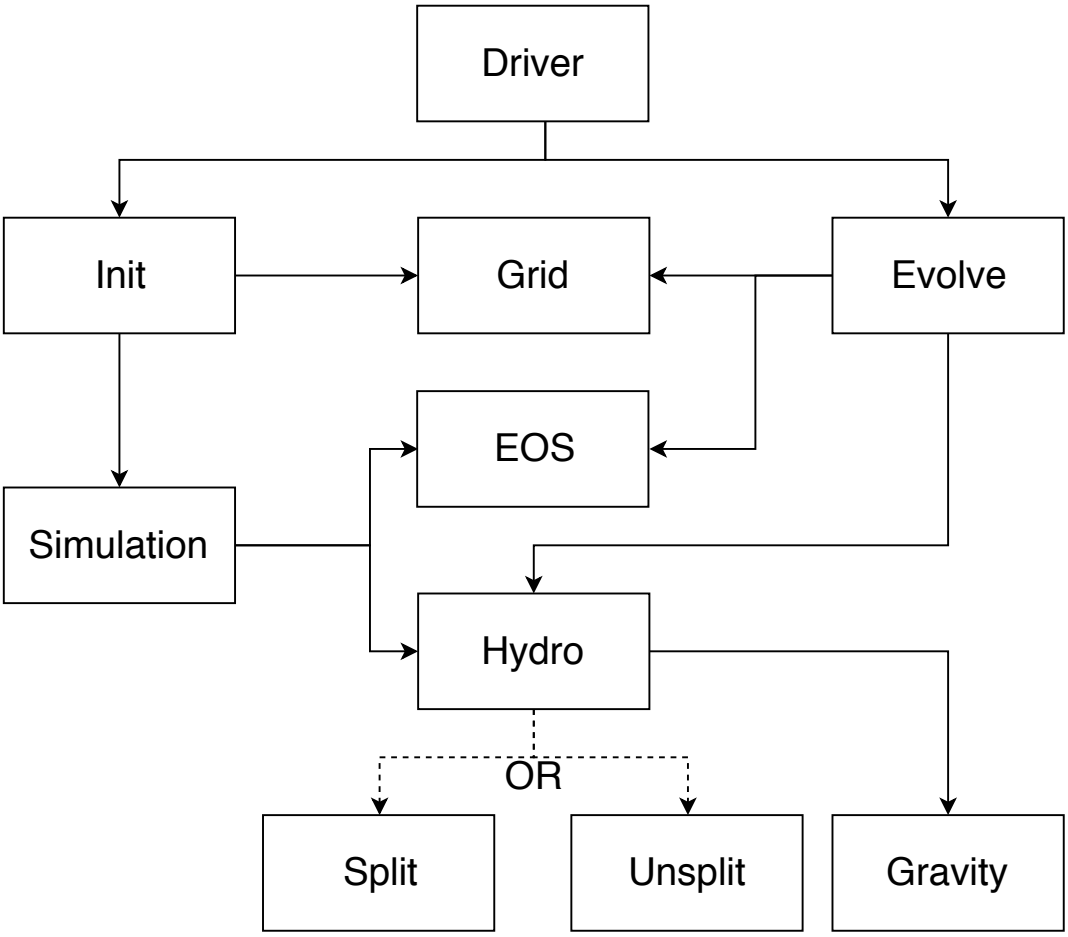

Figure 4.1: Organizational structure of `FLASH`. The Driver unit controls the running of `FLASH` by calling the individual modules in the necessary order, usually configuring the grid, running Hydro (for hydrodynamics) and Gravity, and then computing thermodynamic variables from the EOS. Note the isolated structures in `FLASH`, such that modifying the Hydro unit does not interfere with any other units. The Hydro unit is split into two separate paths consisting of an unsplit and a split method. We modify the unsplit method since it has a straightforward expansion to full MHD.

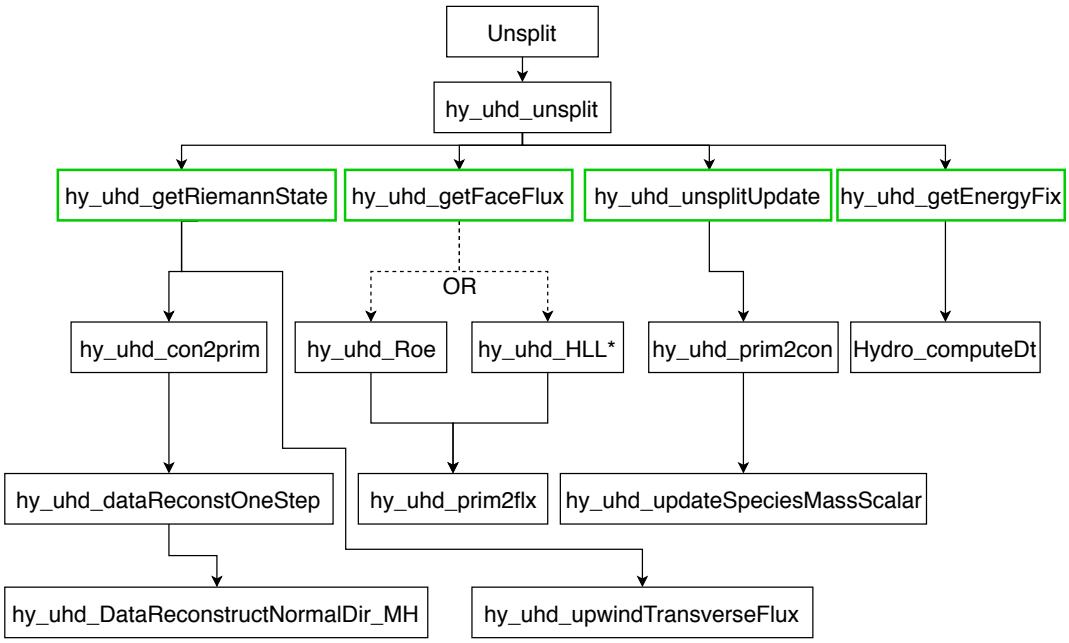

Figure 4.2: Tree diagram showing the flow of the `FLASH` hydrodynamics unit. The main driving file is `hy_uhd_unsplit` which calls upon 4 main subfiles. These are `hy_uhd_getRiemannState`, which does a MUSCL-Hancock expansion of the primitive variables to the faces, `hy_uhd_getFaceFlux`, which converts the primitive variables to fluxes and solves the Riemann problem at each face, `hy_uhd_unsplitUpdate` which updates the cell centered variables using the fluxes at each face, and `hy_uhd_energyFix`, which calculates the new global timestep. These files, modified for spherical coordinates, are highlighted in green. The tasks are further divided into subfiles with their own very specific purpose, such as interconversions of primitive variables, fluxes, and conserved variables or the addition of specific terms in the MUSCL-Hancock expansion.

the geometric source terms are added to the primitive variables when they are expanded to the face. Once we have the states at the face, `hy_uhd_getFaceFlux` converts these to the fluxes of the conserved quantities and then solves the Riemann problem using a supported solver. The final conservative update, handled by `hy_uhd_unsplitUpdate`, takes these fluxes and uses the divergence theorem to advance the volume averaged variables to the next time step. In the reconstruction and conservative update, the finite Cartesian area, volume, and line elements must be replaced by their corresponding spherical components as given in Table A.1 in Appendix §A. The geometric source terms must also be added at both steps, but in the conservative update, we use the explicitly volume averaged ones from equations (3.28)-(3.30). A more general method would be to volume average using numerical quadrature, but the scratch arrays holding the primitive variables at cell faces are not accessible by this routine. The source terms are therefore explicitly integrated for each coordinate system.

During the reconstruction phase, we also have to handle the boundary conditions. It is important that when $\theta \in \{0,\ 180\}$ or $r = 0$, the fluxes in that corresponding direction also vanish with the face area. For reflecting boundary conditions, we ensure that the fluxes in the ghost cells are the exact negative of the fluxes in the domain. This is not natively implemented for spherical coordinates, as setting the primitive velocities in the ghost cells to the negative of the domain velocities no longer results in equal and opposite fluxes being reconstructed. The ghost cells have different geometrical source terms than the domain cells due to their radial and angular dependence, which causes this problem in non-Cartesian geometries. Instead, the routine `hy_uhd_getFaceFlux` is modified to directly set the fluxes in the ghost cells to be equal and opposite. This allows us to test mass and energy conservation in the domain using all reflecting boundaries, as well as providing a framework for reflecting boundary conditions in the even more complex MHD case.

Chapter 5

Code Verification Tests

5.1 Sedov Blast

The Sedov Blast (Sedov, 1959) has widely been used as a test case for hydrodynamic codes. An overpressurized region is created by injecting internal energy into a point at the center of the computational domain, creating a outward going shock wave. This shock wave spreads out, vacating a cavity as it travels. Maintaining the sphericity of the explosion is a strong indicator of a functional code. The semi-analytical solution for the thermodynamic variables at each point in time and space for the purely hydrodynamic situation has the form

$$r = r_2 \lambda, \tag{5.1}$$

$$v = v_2 f, \tag{5.2}$$

$$\rho = \rho_2 g, \tag{5.3}$$

$$p = p_2 h, \tag{5.4}$$

where r is the radius, v is the radial velocity, ρ is the density, p is the pressure, and the subscript 2 indicates the immediate post-shock value of the variable. The functions λ, f, g, h are dependent solely on the geometry, EOS, and initial conditions, and can be found via numerical integration.

We initialize our test explosion with a uniform ambient density of 1, uniform ambient pressure of 1×10^{-5}, and initial energy of 0.85, such that at $t = 1$s the shock radius will be at $r = 1$. This is valid for any consistent unit system (e.g., cgs), given the self-similar nature of the solution.

5.1.1 Finding the Analytic Solution

Initializing the Sedov solution requires finding the density, pressure and velocity pre-shock, post-shock, and at the shock, as outlined in equations (5.1)-(5.4). We follow the methodology of Kamm (2000) for solving the "standard" case with a small but constant ambient pressure and density, and a point source energy deposition. We will briefly detail the process of finding the analytic solution, starting with the HD equations. In 1D, assuming spherical symmetry and a γ-law equation of state, the HD equations can be written as

$$\frac{\partial \rho}{\partial t} + \frac{\partial (\rho v_r)}{\partial r} = \frac{-2\rho v_r}{r}, \tag{5.5}$$

$$\frac{\partial v_r}{\partial t} + v_r \frac{\partial v_r}{\partial r} + \frac{1}{\rho}\frac{\partial p}{\partial r} = 0, \tag{5.6}$$

$$\frac{\partial (p\rho^{-\gamma})}{\partial t} + v_r \frac{\partial (p\rho^{-\gamma})}{\partial r} = 0. \tag{5.7}$$

Sedov showed that by using the self similarity variables V, R and P, implicitly defined as

$$v = \frac{r}{t} V, \tag{5.8}$$

$$\rho = \rho_0 R, \tag{5.9}$$

$$p = \rho_0 \frac{r^2}{t^2} P, \tag{5.10}$$

the above system of equations reduces to one that is only dependent on the initial energy of the shock and the geometry of the problem, such that the

functions $\lambda, f, g,$ and h can be explicitly written as (Kamm, 2000)

$$\lambda = x_1^{-\alpha_0} x_2^{-\alpha_2} x_3^{-\alpha_1}, \tag{5.11}$$

$$f = x_1 \lambda, \tag{5.12}$$

$$g = x_2^{\alpha_3} x_3^{\alpha_4} x_5^{\alpha_5}, \tag{5.13}$$

$$h = x_1^{\alpha_0 j} x_3^{\alpha_4 - 2\alpha_1} x_4^{\alpha_5 + 1}. \tag{5.14}$$

The constants in the above equations are given as

$$x_1 = aV, \tag{5.15}$$

$$x_2 = b(cV - 1), \tag{5.16}$$

$$x_3 = d(1 - eV), \tag{5.17}$$

$$x_4 = b(1 - \frac{c}{\gamma} V). \tag{5.18}$$

In spherical geometry, $j = 3$, and we can further expand the constants in (5.15)-(5.18) as

$$a = \frac{(j+2)(\gamma+1)}{4}, \tag{5.19}$$

$$b = \frac{(\gamma+1)}{(\gamma-1)}, \tag{5.20}$$

$$c = \frac{(j+2)\gamma}{2}, \tag{5.21}$$

$$d = \frac{(j+2)(\gamma+1)}{(j+2)(\gamma+1) - 2(2 + j(\gamma-1))}, \tag{5.22}$$

$$e = \frac{2 + j(\gamma-1)}{2}, \tag{5.23}$$

and the exponents in (5.11)-(5.14) are given as

$$\alpha_0 = \frac{2}{j+2}, \tag{5.24}$$

$$\alpha_1 = \frac{(j+2)\gamma}{2+j(\gamma-1)}\left(\frac{2j(2-\gamma)}{\gamma(j+2)^2} - \alpha_2\right), \tag{5.25}$$

$$\alpha_2 = \frac{1-\gamma}{2(\gamma-1)+j}, \tag{5.26}$$

$$\alpha_3 = \frac{j}{2(\gamma-1)+j}, \tag{5.27}$$

$$\alpha_4 = \frac{j(j+2)}{j(2-\gamma)}\alpha_1, \tag{5.28}$$

$$\alpha_5 = \frac{2j}{j(\gamma-2)}. \tag{5.29}$$

To find the solution we need only the function λ (5.11), after which the rest of the functions can be calculated from it. λ is determined by using the similarity relation from dimensional analysis of the explosion, which says that the shock radius and speed are related to the energy of the shock via

$$r_2 = \left(\frac{E_0}{\rho_0 \kappa}\right)^{1/(j+2)} t^{2/(j+2)}, \tag{5.30}$$

$$v_s = \frac{\partial r_2}{\partial t} = \frac{2}{j+2}\left(\frac{r_2}{t}\right), \tag{5.31}$$

where the constant of proportionality κ is once again reliant on only the total energy of the shock and the geometry. We determine κ by using the self similarity variables to calculate the integrals defining the total energy of the system

$$E_0 = \int_0^{r_2} \frac{1}{2}\rho v^2 \mathrm{d}V + \int_0^{r_2} \frac{p}{\gamma-1}\mathrm{d}V. \tag{5.32}$$

From here, the self similar kinetic energy integral is defined as J_1, the internal energy is J_2, and it can be shown that these are equal to

$$J_1 = \frac{\gamma+1}{1-\gamma}V^2\left(\frac{\alpha_0}{V} + \frac{\alpha_2 c}{cV-1} - \frac{\alpha_1 e}{1-eV}\right) \left([aV]^{\alpha_0}[b(cV-1)]^{\alpha_2}[d(1-eV)]^{\alpha_1}\right)^{-(j+2)} \left([b(cV-1)]^{\alpha_3}[d(1-eV)]^{\alpha_4}[b(1-\frac{c}{\gamma}V)]^{\alpha_5}\right) \tag{5.33}$$

and

$$J_2 = \frac{(cV-\gamma)(\gamma-1)}{(1-cV)2\gamma}J_1. \tag{5.34}$$

Both J_1 and J_2 are integrated numerically from the velocity at the center until the outer edge of the shock, corresponding to the self similar variables V_0 to V_S. These are found by replacing the appropriate radii, velocities, and times into the self similar solutions, yielding

$$V_0 = \frac{2}{(\gamma-1)(j+2)}, \tag{5.35}$$

$$V_S = \frac{4}{(j+2)(\gamma+1)}. \tag{5.36}$$

The constant proportionality constant for the energy, κ in (5.30), is given as

$$\kappa = 2^{j-2}\pi J_1 + \frac{2^{j-1}}{\gamma-1}\pi J_2. \tag{5.37}$$

$$\tag{5.38}$$

If $j = 1$, for Cartesian geometry, then the geometry no longer has curvature, and we divide by a factor of π to account for this change in length.

To determine the rest of the immediate post shock values, we use Rankine-

Hugoniot relations for a strong shock, giving the results

$$v_2 = \frac{2}{\gamma+1} v_s, \tag{5.39}$$

$$\rho_2 = \frac{\gamma+1}{\gamma-1} \rho_0, \tag{5.40}$$

$$p_2 = \frac{2}{\gamma+1} \rho_0 v_s^2. \tag{5.41}$$

Care and precision must be taken when numerically integrating the self similar energies, J_1 and J_2, as a singularity occurs at the lower bound of the integral, V_0. We use Simpsons rule with 1000 points, which allows us to approach the singularity to a lower bound of $V_0 + 1.256 \times 10^{-6}$. Implementing this matches the results of Kamm (2000) for an initial energy of $E_0 = 0.851072$. Additionally, finding the function λ numerically near the singularity requires careful work with Newton-Raphson (NR) iterations. We implement this by limiting our NR slope by a factor of 100 once we approach $r = 0.5$.

5.1.2 Sedov Blast Results

We generate the initial explosion by reading in the analytic solution for these conditions at $t = 0.04$ s, and then allow the code to evolve the solution independently. In Figure 5.1 we show a snapshot of the Sedov explosion at 0.14 s, noting that the explosion retains its sphericity despite the θ dependence of geometric source terms. Furthermore, we overlay the azimuthally and polar averaged thermodynamic variables extracted from our simulation at a time of 0.14 s and 0.93 s with the analytic solutions in Figure 5.2. At the earlier time, the simulation is plagued by a transient reverse pressure wave, noticeable in the velocity and pressure gradients. However, the steepness of the shock is well preserved across 2-3 cells. At later times, the transient wave reflects off the interior boundary and dissipates once it hits the forward shock. Small differences in the density in the post shock region are caused by the finite density floor

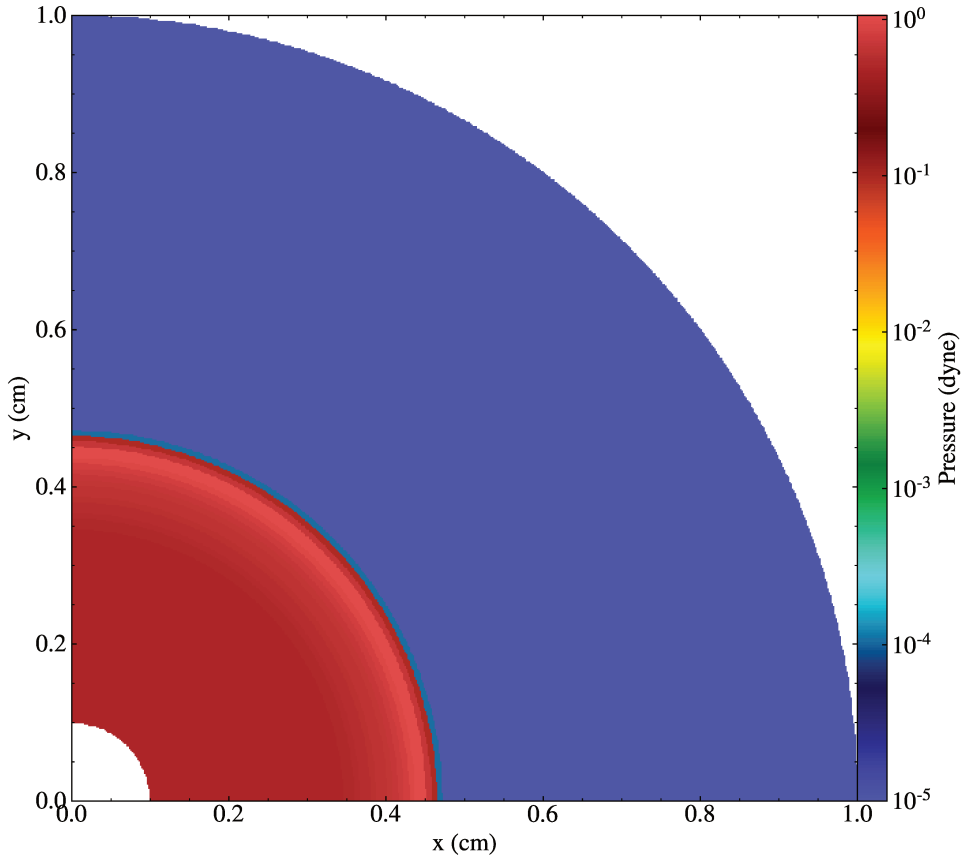

Figure 5.1: Equatorial snapshot of the outgoing pressure wave from the Sedov blast at $t = 0.14$ s. The wave remains symmetric throughout the simulation, and the shock position is clearly defined by 2 or 3 cells.

required for numerical reasons, while the analytic solution completely vacates the cavity. To ensure the code is conservative, we initialize the domain with reflecting boundary conditions in 3 dimensions and track the global energy and mass. Figure 5.3 shows the normalized differences in energy and mass,

$$\Delta\hat{E} = \frac{E - E_0}{E_0}, \tag{5.42}$$

$$\Delta\hat{M} = \frac{M - M_0}{M_0}, \tag{5.43}$$

where M_0 and E_0 are the initial total mass and energy in the domain, M and E are the instantaneous global values for each time step. The total evolution

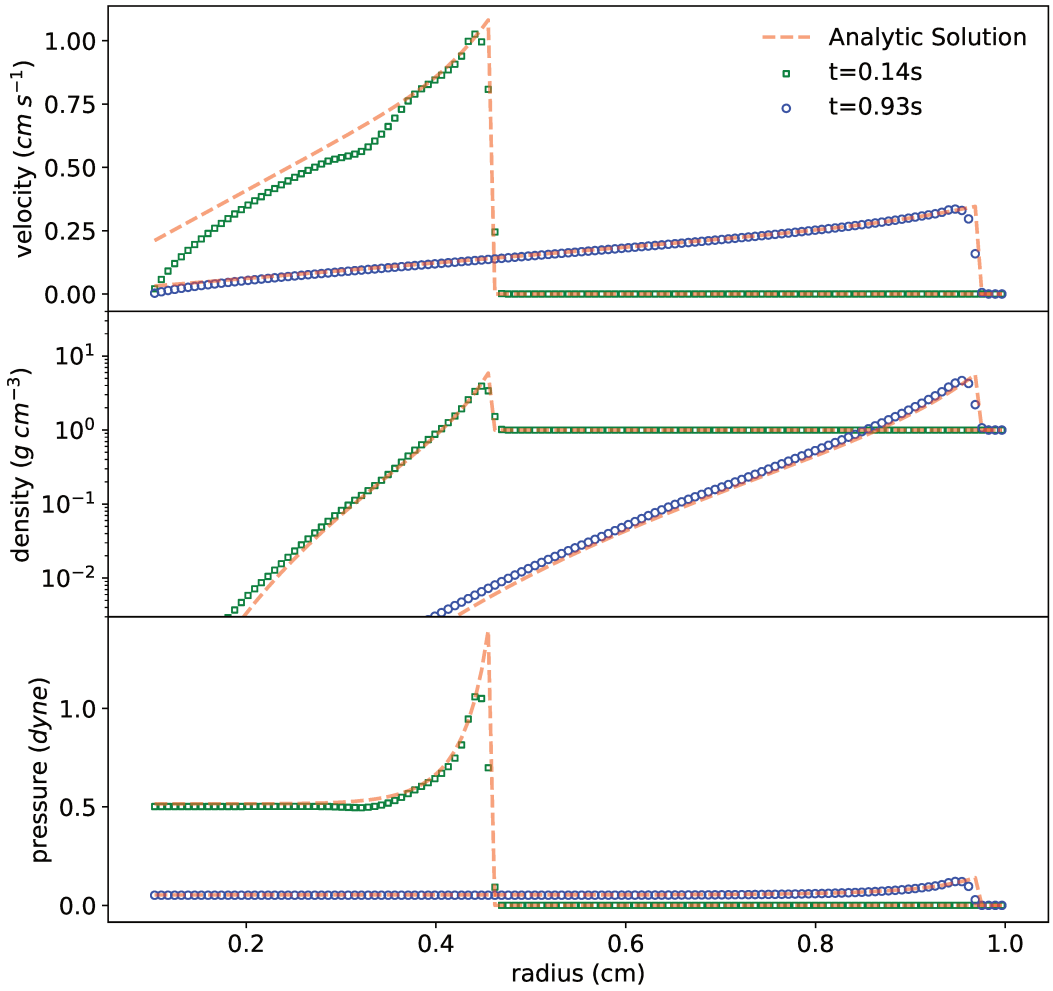

Figure 5.2: Analytic (dashed) and FLASH angle-averaged 3D (dotted) solutions to the Sedov explosion problem. The initial solution is read in by FLASH at a time of 0.04 s, and then the shock is evolved. A transient pressure wave, an artefact of finite resolution, is visible at early times, but dissipates as it hits the shock. The shock is resolved by 2-3 cells at all times, and our finite resolution prevents the simulation from reaching the peak analytic values in each variable.

consists of about 7000 individual steps. Both mass and energy are conserved to the same level as the Cartesian implementation in `FLASH`. This shows that despite the source terms not being equal in each cell due to the radial and polar dependence, the fluxes at each face still have near perfect cancellation globally.

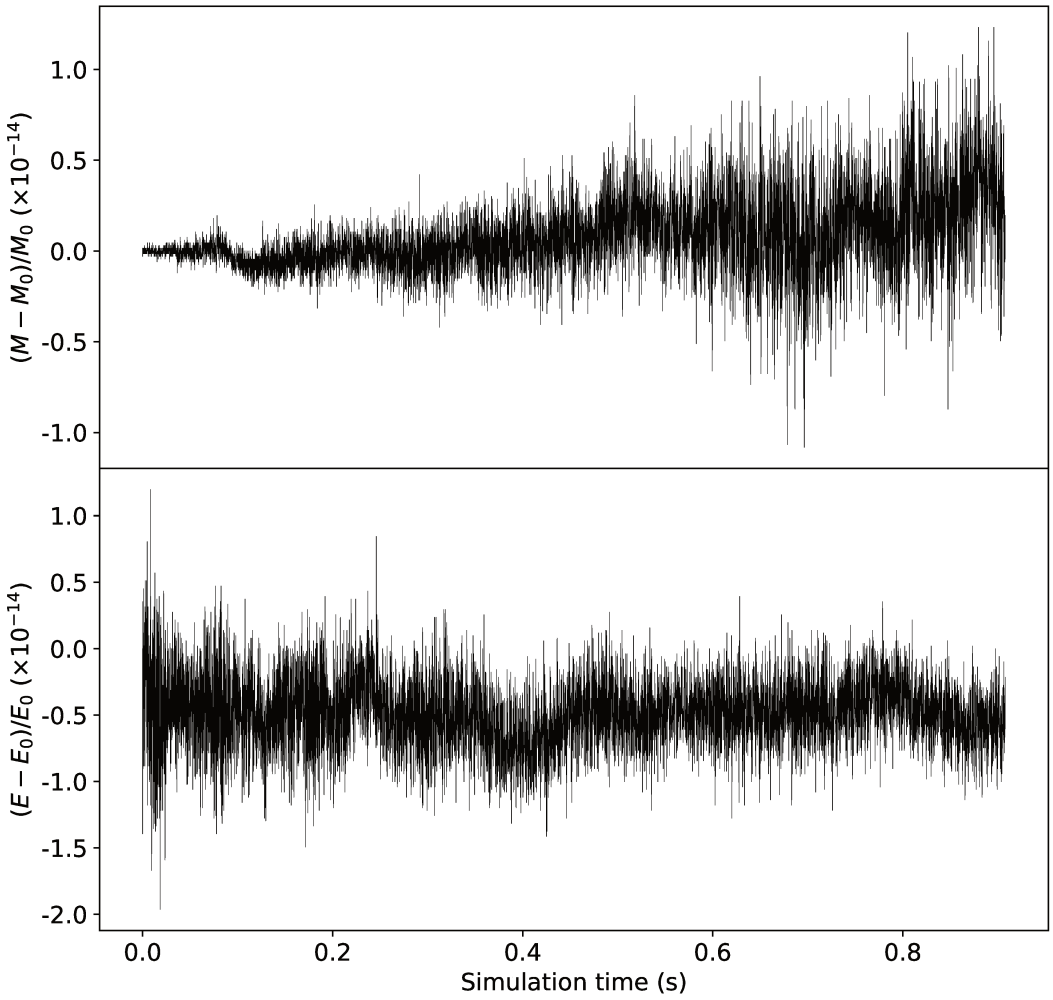

Figure 5.3: Conservation of global mass (top) and energy (bottom) over ∼7000 timesteps to machine precision, with no discernible pattern. Values are plotted as differences from the original simulation values, as given in (5.42) and (5.43). This is an important test of the perfect cancellation of fluxes at cell boundaries, even with the addition of the geometric source terms (which are cell centered, not face centered).

5.2 Equilibrium Torus

Previous works on binary NS mergers have used an equilibrium torus surrounding a compact object to approximate the state of the disk after the metric has settled into a nearly stationary configuration. It is therefore both a useful step in continuing research to set up an initial torus to which we can later

add additional microphysics modules, in particular neutrino heating and nuclear recombination. Equilibrium tori are also steady-state solutions to the HD equations, so we can use them to test our code since a torus orbiting a point mass should retain its equilibrium state over multiple orbits. Sections §5.2.1-5.2.5 describe the construction of the torus around a spinning compact object in great detail, due to its importance in future work, while we discuss the results of the test in §5.2.7.

5.2.1 Initializing the Torus

If we take the compact object to be a point mass, a good approximation for NS mergers since the remnant contains $\gtrsim 95\%$ of the mass, then we can define a gravitational potential quite easily. After that, we choose 4 parameters: The radius the torus forms at and its mass, R_0 and M_t, as well as the entropy and electron fraction of the torus material, s_0 and $Y_{e,0}$. These parameters will yield a unique dimensionless distortion parameter, d, which sets the cross sectional area, or shape, of the torus. Following Papaloizou and Pringle (1984) and using Bernoulli's principle, we define the equilibrium equation as a sum of enthalpy and the rotational kinetic energy and gravitational potentials, which will be equal to a constant,

$$w + \Phi_g + \Phi_{\rm rot} = C. \tag{5.44}$$

For bound torus configurations, the constant $C < 0$. Equivalently if we write the rotational kinetic energy as a function of the specific angular momentum, $\Phi_{rot} = \ell^2/2r_{\rm cyl}^2$, such that we recover Keplerian rotation in the absence of gas pressure, we have

$$w = -\Phi_g - \frac{\ell^2}{2r_{\rm cyl}^2} + C. \tag{5.45}$$

To model the spinning gravity of a compact object, we use the pseudo-Newtonian potential of Artemova et al. (1996), which can be written outside

the event horizon as (Fernández et al., 2015)

$$\Phi_A = \begin{cases} \frac{GM}{r_1(\beta-1)}\left[1 - \left(\frac{r}{r-r_1}\right)^{\beta-1}\right], & \beta \neq 1 \\ \frac{GM}{r_1}\ln\left(1 - \frac{r_1}{r}\right), & \beta = 1 \end{cases}, \tag{5.46}$$

where M is the black hole mass, and r_1 is the event horizon. The parameter β relates the event horizon and innermost stable circular orbit (ISCO) as

$$\beta = \frac{r_{\mathrm{ISCO}}}{r_1} - 1, \tag{5.47}$$

where the ISCO is defined as in the Kerr metric. The gravitational acceleration at any point is

$$\frac{\mathrm{d}\Phi_{\mathrm{A}}}{\mathrm{dr}} = \frac{GM}{r^{2-\beta}(r-r_1)^{\beta}}, \tag{5.48}$$

and the event horizon is located at

$$r_1 = \frac{GM}{c^2}(1 + \sqrt{1-a^2}), \tag{5.49}$$

where a is the dimensionless spin parameter. To obtain the constant specific angular momentum, we define $\ell = r^2\omega$ to once again yield Keplerian rotation and using

$$\omega^2 = \frac{1}{r}\frac{\mathrm{d}\Phi}{\mathrm{dr}}, \tag{5.50}$$

and then applying this to the Artemova potential, we find

$$\ell^2 = r^3\left[\frac{GM}{r^{2-\beta}(r-r_1)^{\beta}}\right],$$

which reduces to

$$\ell^2 = GM\frac{r^{\beta+1}}{(r-r_1)^{\beta}}. \tag{5.51}$$

Angular momentum must be conserved once the material that forms the torus passes the circularization radius. Therefore, the torus can be constructed with constant angular momentum of

$$\ell^2 = GM \frac{R_0}{(1 - r_1/R_0)^\beta}, \tag{5.52}$$

which in turn makes the azimuthal angular velocity

$$\begin{aligned} v_\phi &= \frac{\ell}{r_{\text{cyl}}} \\ &= \left(\frac{GM}{R_0} \frac{1}{r_{\text{cyl}}^2 (1 - r_1/R_0)^\beta} \right)^{\frac{1}{2}}. \end{aligned} \tag{5.53}$$

If we substitute this back into equation (5.45) using the Artemova potential, equation (5.46), we get

$$w = \frac{-GM}{r_1(\beta - 1)} \left[1 - \left(\frac{r}{r - r_1} \right)^{\beta - 1} \right] - \frac{GMR_0}{2r_{\text{cyl}}^2 (1 - r_1/R_0)^\beta} + C. \tag{5.54}$$

The constant C is determined by the radial boundaries of the torus (see Papaloizou and Pringle, 1984), and can be defined in terms of the distortion parameter, d, a measurement of the shape of the torus,

$$d = \frac{r_- + r_+}{2R_0} = -\frac{1}{2C}. \tag{5.55}$$

Real solutions only exist when $d > 1$, or the torus limits are not physical. We can put this into (5.54) and factor out GM/R_0 to get

$$w = \frac{GM}{R_0} \left\{ \frac{-R_0}{r_1(\beta - 1)} \left[1 - \left(\frac{r}{r - r_1} \right)^{\beta - 1} \right] - \frac{R_0^2}{2r_{\text{cyl}}^2} \left(\frac{R_0}{R_0 - r_1} \right)^\beta - \frac{1}{2d} \right\}. \tag{5.56}$$

We now have the enthalpy at every point in the torus, dependent on only the circularization radius, gravitational potential, and the free distortion parameter. What we want, however, is to choose a torus mass that fits our chosen

parameter space. We use the limits of the torus to define the mass as

$$M_t = \int_0^{2\pi} \int_{z_{\rm lo}}^{z_{\rm hi}} \int_{r_{\rm lo}}^{r_{\rm hi}} \rho(w) r_{\rm cyl} {\rm d}r_{\rm cyl} {\rm d}z {\rm d}\phi. \tag{5.57}$$

To do this, we need to find the density solely as a function of enthalpy, entropy and electron fraction, all of which we know (or can choose) at each point. Succinctly, we would like

$$\rho = \rho(w \mid s, Y_e). \tag{5.58}$$

We can do this by inverting the enthalpy for a given entropy and composition (equivalently electron fraction, since all other mass fractions can be determined from there using nuclear statistical equilibrium). All that remains after that is to find the bounds of the torus (see §5.2.3-5.2.4), and then integrate the density within them to find the torus mass.

If the integration does not return the torus mass that we are looking for, we will change the shape (and therefore mass) by modifying d, using NR iteration to recalculate the enthalpies and torus mass. Through iteration, we will find the torus mass that we want, and we can then use the corresponding value of the distortion parameter and the corresponding enthalpies to create our desired density function, (5.58). Then using the found density, chosen entropy, and chosen Y_e we can construct a torus with consistent thermodynamic variables.

5.2.2 Helmholtz EOS

`FLASH` natively supports analytic γ-law type equations of state, and also the Helmholtz EOS of Timmes and Swesty (2000). The Helmholtz EOS is a tabulated EOS that includes pressure contributions from radiation, an ideal gas of ions (including Coulomb corrections), and an electron/positron gas with any arbitrary degeneracy and relativity parameter. It covers the thermodynamic

range of 10^{-10} g cm^{-3} $< \rho <$ 10^{11} g cm^{-3} and 10^4 K $< T <$ 10^{11} K. The density and temperature upper bounds can be expanded by the inclusion of an analytic degenerate relativistic electron/positron gas (Fernández and Metzger, 2013; Bethe et al., 1980). This covers a broad parameter space necessary for the varying conditions required in the aftermath of a NS merger. The Helmholtz EOS has been previously modified to support effects of nuclear recombination (Fernández and Metzger, 2013) and only minor tweaks were made to update this functionality to work in `FLASH4.5`.

We can construct our torus using the Helmholtz EOS with the following recipe. At each point in the torus we calculate the enthalpy for a choice of gravitational potential and torus mass, given by (5.56). At this point, we want to find the temperature given the density, enthalpy, and composition. However, there is no function that inverts the EOS in this way, since the tabulated electron quantities require a temperature to interpolate. We solve this by computing the EOS at a density, entropy, and composition, which returns a guess at the enthalpy w_g. If this guess at the enthalpy does not match the determined enthalpy, then we iterate over the temperature until we converge on the correct enthalpy. We do this by starting with the definition of enthalpy,

$$w = e + P/\rho, \tag{5.59}$$

or to make our NR efficient, we can normalize

$$0 = \frac{(e + P/\rho)}{w} - 1. \tag{5.60}$$

Then we change the temperature to find the correct thermodynamic variables, since we can do

$$T = T - w \Big/ \left(\frac{\mathrm{d}w}{\mathrm{d}T}\right)_{s,Y_e}, \tag{5.61}$$

but the Helmholtz EOS does not calculate $\mathrm{d}w/\mathrm{d}T$, so we can expand it out as

$$\left(\frac{\mathrm{d}w}{\mathrm{d}T}\right)_{s,Y_e} = \left(\frac{\mathrm{d}e}{\mathrm{d}T}\right)_{s,Y_e} + \frac{1}{\rho}\left(\frac{\mathrm{d}P}{\mathrm{d}T}\right)_{s,Y_e} - \frac{P}{\rho^2}\left(\frac{\mathrm{d}\rho}{\mathrm{d}T}\right)_{s,Y_e} \tag{5.62}$$

This can be further expanded out in terms of partial derivatives that the Helmholtz EOS does calculate, since for a fixed composition, $P = P(\rho, T)$, $E = E(\rho, T)$, and $\rho = \rho(s, T)$:

$$\left(\frac{\mathrm{d}\rho}{\mathrm{d}T}\right)_{s,Y_e} = \left(\frac{\partial\rho}{\partial T}\right)_{s,Y_e} + \left(\frac{\partial\rho}{\partial s}\right)_{T,Y_e}\left(\frac{\partial s}{\partial T}\right)_{\rho,Y_e}, \tag{5.63}$$

$$\left(\frac{\mathrm{d}e}{\mathrm{d}T}\right)_{s,Y_e} = \left(\frac{\partial e}{\partial T}\right)_{s,Y_e} + \left(\frac{\partial e}{\partial \rho}\right)_{s,Y_e}\left(\frac{\partial\rho}{\partial T}\right)_{s,Y_e}, \tag{5.64}$$

$$\left(\frac{\mathrm{d}P}{\mathrm{d}T}\right)_{s,Y_e} = \left(\frac{\partial P}{\partial T}\right)_{s,Y_e} + \left(\frac{\partial P}{\partial \rho}\right)_{s,Y_e}\left(\frac{\partial\rho}{\partial T}\right)_{s,Y_e}. \tag{5.65}$$

All of the derivatives on the right hand side are quantities that are calculated by the Helmholtz EOS, so we can use this process to find the enthalpy given that we do not know the temperature.

5.2.3 Finding the Radial Limits

In order to construct the torus, we have to know the radial limits. We know that at the zero-enthalpy surface, there is no pressure, and this gives the limits of the torus. If we set $z = 0$ in the enthalpy equation, we solve for the cylindrical radial boundaries, so $r = r_{\mathrm{cyl}}$ and therefore

$$0 = \frac{R_0}{r_1(\beta-1)}\left[1 - \left(\frac{r_{\mathrm{cyl}}}{r_{\mathrm{cyl}} - r_1}\right)^{\beta-1}\right] - \frac{R_0^2}{2r_{\mathrm{cyl}}^2}\left(\frac{R_0}{R_0 - r_1}\right)^{\beta} - \frac{1}{2d}. \tag{5.66}$$

We use NR again to quickly find the root. To make this computationally efficient, we want to normalize the above equation in units of R_0, so we define

$$r_s = r_1/R_0, \tag{5.67}$$

$$\tilde{\omega}_s = r_{\rm cyl}/R_0, \tag{5.68}$$

which yields

$$f = \frac{1}{r_s(\beta-1)}\left[1-\left(\frac{\tilde{\omega}_s}{\tilde{\omega}_s - r_s}\right)^{\beta-1}\right] - \frac{1}{2\tilde{\omega}_s^2}\left(\frac{1}{1-r_s}\right)^{\beta} - \frac{1}{2d}, \tag{5.69}$$

and the derivative for the NR iterations is therefore

$$f' = -\frac{1}{\tilde{\omega}_s^2}\left(\frac{\tilde{\omega}_s}{\tilde{\omega}_s - r_s}\right)^{\beta} + \frac{1}{\tilde{\omega}^3}\left(\frac{1}{1-r_s}\right)^{\beta}, \tag{5.70}$$

5.2.4 Finding the z-Limits

At each radius between these two radial limits, we have to find the upper z-limit by using NR iterations until the enthalpy vanishes, since that is the torus edge. We assume equatorial symmetry and set the lower z-limit to be the same as the upper one. This is done through the same process, except now our normalized function to iterate over is

$$f = \frac{1}{r_s(\beta-1)}\left[1-\left(\frac{1}{(\tilde{\omega}_s^2+\tilde{z}^2)^{\frac{1}{2}}}\right)^{\beta-1}\right] - \frac{1}{2\tilde{\omega}_s^2}\left(\frac{1}{1-r_s}\right)^{\beta} - \frac{1}{2d}, \tag{5.71}$$

and we instead iterate over $\tilde{z}$, defined in units of R_0 as above. Now, we find the derivative

$$f' = \frac{r_s^{\beta-2}}{(r_s-r)^{\beta}}\frac{\tilde{z}}{(\tilde{\omega}_s^2+\tilde{z}^2)^{\frac{1}{2}}}, \tag{5.72}$$

and then we have all the pieces to perform the NR for the z-limits. Convergence in the root finder is sensitive to the initial seed value. To get around this, we do one run of the whole torus, finding the z-limits iteratively. Each limit is used as

a seed to find the next one, which works well as there is not much iteration over such a small change. Additionally, converging on a solution becomes difficult when the inner radial limit approaches the ISCO.

5.2.5 Ambient Medium

We want to set up a medium that is in hydrostatic equilibrium, such that

$$\mathrm{d}P = -\rho(r)g(r)\mathrm{d}r. \tag{5.73}$$

The density profile is set to be radially decreasing, so $\rho = \rho_0 r^{-\lambda}$. Since the central point mass dominates the gravitational profile, hydostatic equilibrium is approximately satisfed by imposing

$$P(r) = -\rho\phi_A, \tag{5.74}$$

which neglects factors arising from the analytic integration of (5.73), and where ϕ_A is given by the Artemova potential (5.46). We can convert this to a temperature using radiation pressure, which dominates the EOS at this point,

$$T = \left(\frac{3P}{a}\right)^{1/4}, \tag{5.75}$$

where a is the radiation constant. This temperature is used as the temperature seed for the Helmholtz EOS iteration in the ambient medium. Slight deviations from hydrostatic equilibrium do not dynamically affect the outflow, as the ambient density profile is normalized to a small fraction of the torus (see §2.1.1).

5.2.6 Gamma Law Torus

Initializing a torus using both the Helmholtz EOS and Artemova potential brings in factors that can disrupt equilibrium, like strong gravitational effects

near the ISCO. As a simple code test, we also initialize a torus in Newtonian gravity using a γ-law EOS. This is done by following the same steps as for the Artemova potential, but we insert a Newtonian gravitational potential, which gives our equilibrium equation as

$$\frac{P}{\rho}(n+1) = \frac{GM}{R_0}\left(\frac{R_0}{r} - \frac{R_0^2}{2r_{\rm cyl}^2} - \frac{1}{2d}\right). \tag{5.76}$$

where $n = (\gamma - 1)^{-1}$ and we have replaced the enthalpy with pressure and density as in (5.59). Using the point of maximum density, at a cylindrical radius of R_0, and then applying the γ-law EOS to say $P = A\rho^\gamma$, we can find the constant A

$$A = \frac{GM}{R_0(n+1)\rho_0^{1/n}}\left(\frac{d-1}{2d}\right). \tag{5.77}$$

Two quadratic equations define the r- and z-limits, respectively written as

$$r_\pm = d \pm \sqrt{d(d-1)} \tag{5.78}$$

$$z_\pm = \pm\frac{r_{\rm cyl}}{d + r_{\rm cyl}^2}\sqrt{4(r_{\rm cyl}d)^2 - d^2 - 2r_{\rm cyl}^2 d - r_{\rm cyl}^4} \tag{5.79}$$

Since the limits are analytic expressions and there is no ISCO, it is much easier to form a torus at any radius using the Newtonian potential. The density at each point is found by rearranging the equilibrium equation (5.76), and then the pressure is found using the EOS,

$$\rho = \left[\frac{GM}{R_0(n+1)A}\left(\frac{R_0}{r} - \frac{R_0^2}{2r_{\rm cyl}^2} - \frac{1}{2d}\right)\right]^n, \tag{5.80}$$

$$P = A\rho^\gamma. \tag{5.81}$$

5.2.7 Torus Test Results

The Helmholtz EOS torus with the Artemova potential is evolved for 5 orbits, using the radius of maximum density in the torus, $R_0 = 50$ km, a gravitational mass of $2.65\,M_\odot$, and a non spinning BH, which determines the parameter β and the location of the event horizon, r_1. Spin, mass, electron fraction, and entropy of the torus are chosen as 0, $0.1\,M_\odot$, 0.1, and 8 k_b baryon^{-1} respectively, to match a previously ran 2D case for comparison. The Keplerian orbital timescale at R_0 is given by

$$t = 2\pi\sqrt{\frac{R_0^3}{GM}}(1 - r_1/R_0)^{\beta/2} \approx 3.7 \text{ ms}, \tag{5.82}$$

where the additional correction factor to the Newtonian timescale comes from the use of the Artemova potential (see §5.2.1).

A snapshot of the torus density at $t = 0$ and $t = 18.5$ ms (5 orbits) is shown in Figures 5.4 and 5.5. After a few orbits, the torus begins to puff up and accrete, as the sharp pressure gradient between the torus and ambient cannot be maintained and diffusion begins. This variation contains $< 2\%$ of the initial torus mass, thus $> 98\%$ of the mass remains unchanged. This demonstrates the ability of the code to advect supersonically in the $\hat{\phi}$ direction, with little numerical viscosity. The accretion noticeable in the torus is most likely due to strong gravitational effects near the ISCO. To remove this effect, we initialize a γ-law torus an order of magnitude further out (500 km) in a Newtonian potential, shown in Figure 5.6. The mass of this torus is $0.04\,M_\odot$, necessary for equilibrium, and the other torus parameters remain unchanged. In this setup $< 0.05\%$ of the torus diffuses or accretes, showing how without strong gravitational effects, the torus holds equilibrium much better. These tests also show the compatibility of the code with additional physical source terms, as gravity holds the torus in place correctly. Unfortunately, Figure 5.7 shows that gravity decreases the accuracy of energy conservation to order 10^{-3}. This is

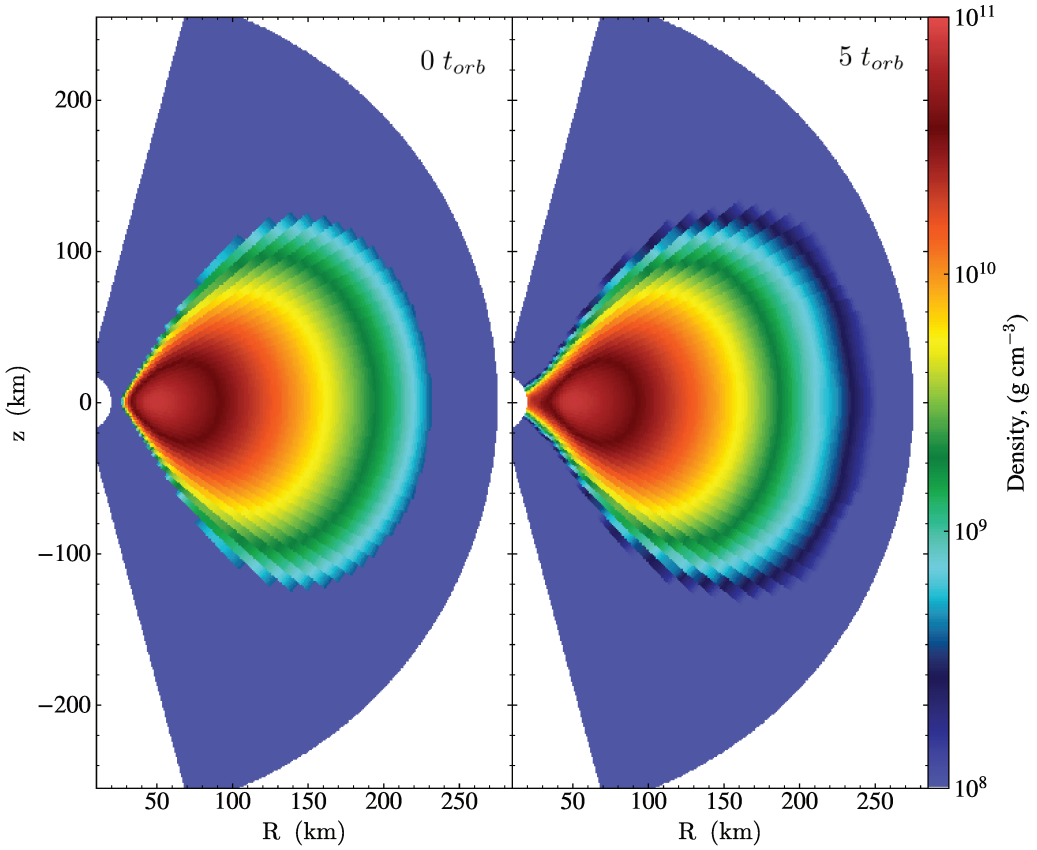

Figure 5.4: Meridionial slices of the torus density in its initial state, and then after ∼5 orbits. Diffusion occurs along the sharp pressure gradient at the torus edges, but $> 98\%$ of the mass stays within the defined torus limits, despite mass advecting supersonically in the $\hat{\phi}$ direction. Accretion onto the central object is likely due to the disruption of equilibrium by the strong gravitational potential felt near the ISCO, which is located at $\sim$ 23 km. The simulation inner boundary is located at $r = 20$ km, between the ISCO and event horizon.

due to the approximation of gravitational energy as

$$U_g = -\int_V \rho(r)\frac{GM}{r}\mathrm{d}V \approx -\rho\frac{GM}{r}\Delta V. \tag{5.83}$$

Performing the integration for

$$\rho(r) = \rho + \frac{\Delta r}{2}\frac{\partial \rho}{\partial r}, \tag{5.84}$$

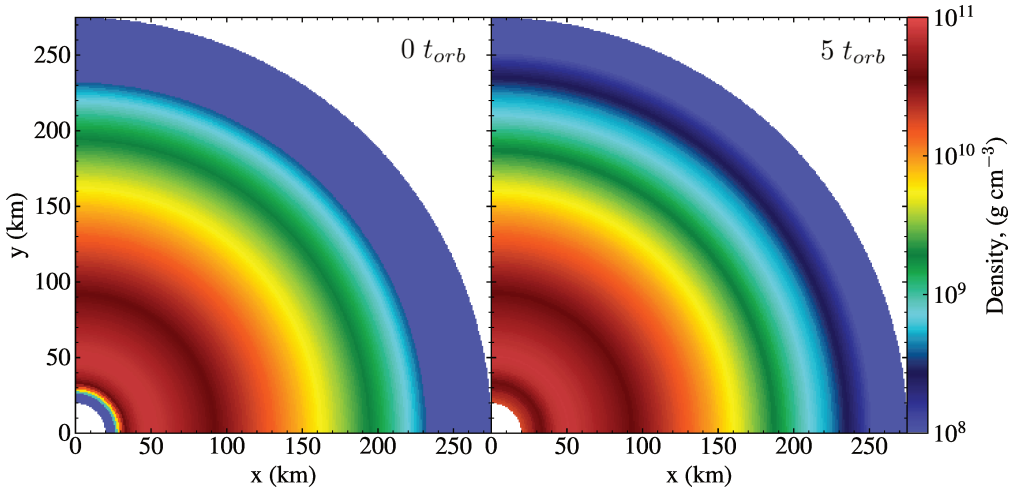

Figure 5.5: Same as Figure 5.4 except a top down view of the equatorial plane.

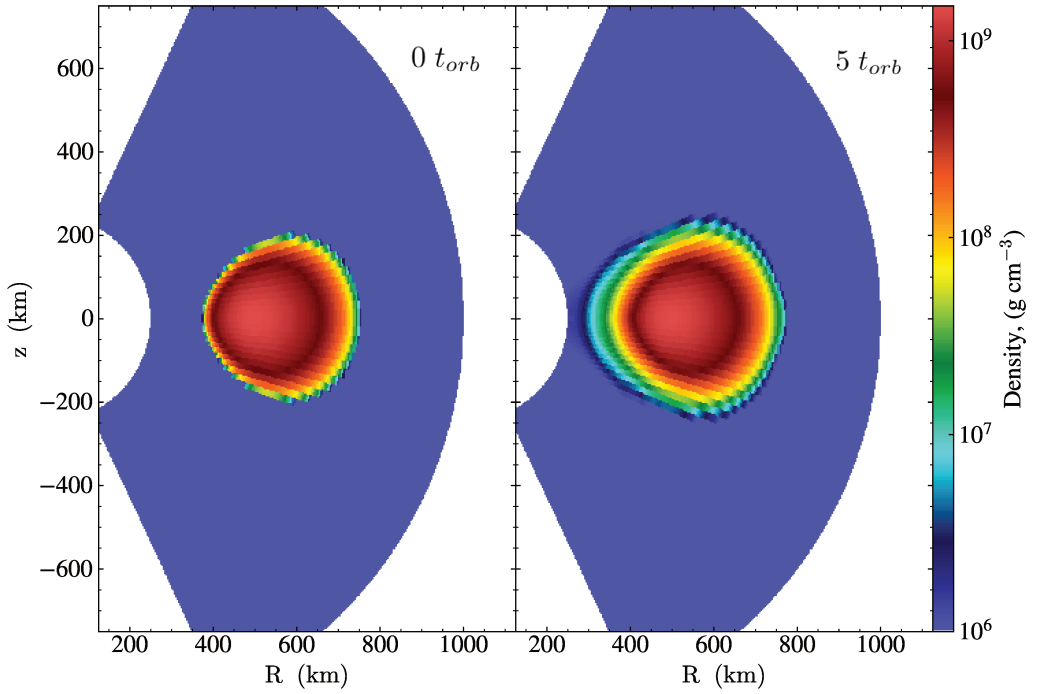

Figure 5.6: Meridional slices of the γ-law torus density in its initial state, and then after $\sim$5 orbits. The lack of an ISCO in the Newtonian gravitational potential, combined with the torus being formed at 500 km out allows for much better equilibrium than the Helmholtz Artemova torus. $>$ 99% of the torus mass stays in its initial position.

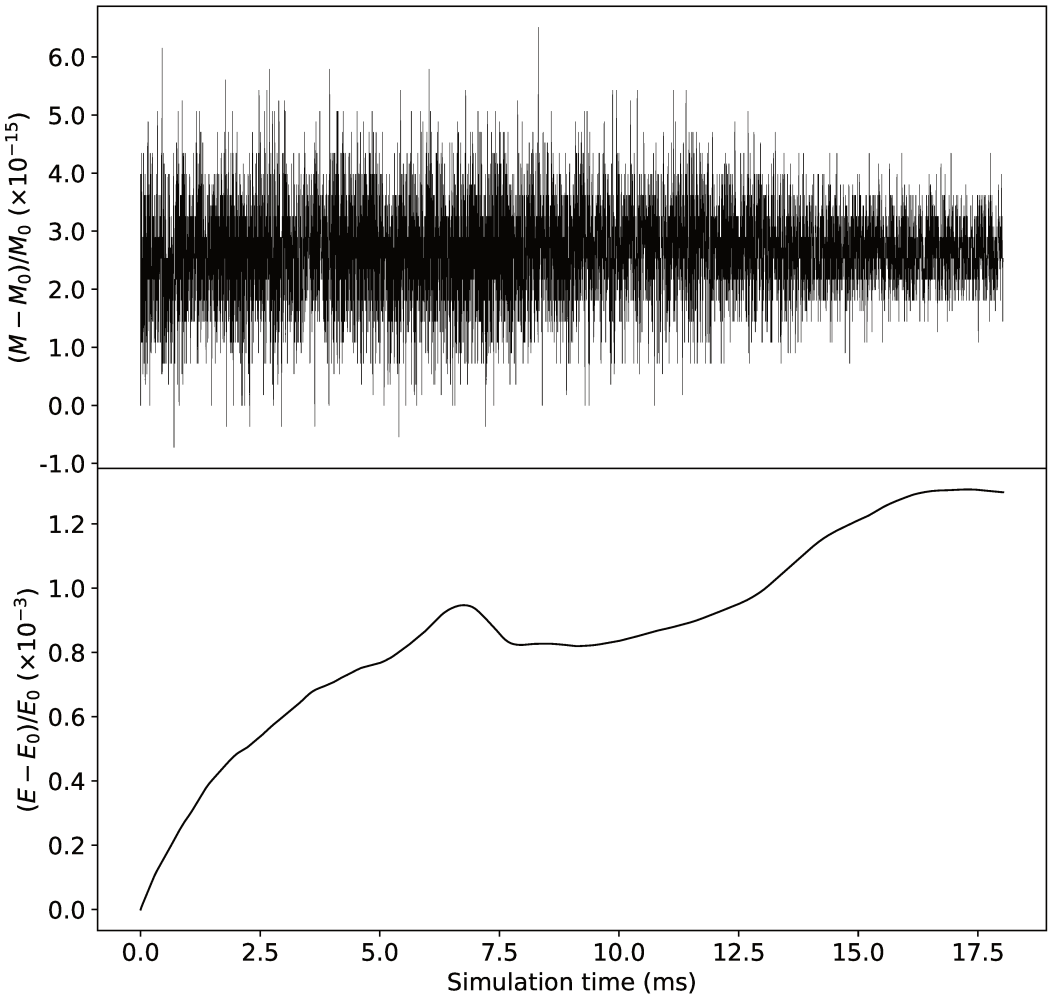

Figure 5.7: Global mass (top) and energy (bottom) difference from the original simulation values over ∼8000 timesteps of the Helmholtz torus, defined in the same way as for the Sedov explosion. Mass is conserved to machine precision, while energy is not due to the implementation of calculating the gravitational energy over a cell in `FLASH`. The γ-law torus displays the exact same trends. Both show energy errors on the expected order of magnitude ($\sim 10^{-4}$) and changes with time corresponding to global shifts in mass (see text for details).

we find it is expected to introduce errors on the order of $r\Delta(r^2)/\Delta(r^3)$ for PLM. Comparison to results show this is the case, taking the radius R_0 where density is maximal, gives this error as 10^{-4}. Since the majority of mass is all moving in one direction, towards smaller r, the errors are expected to accumulate with time. Importantly, we note that mass is still conserved to machine precision.

Chapter 6

Conclusion

In this thesis we simulated the post-merger state of binary NS mergers. We began modeling 2 dimensional axisymmetric tori around a HMNS with computationally efficient parameterizations of the relevant microphysics, including gravity, neutrino interactions, nuclear recombination and viscous stresses. We found that it is problematic to recreate the high ($\sim 0.3c$) lanthanide-free ejecta velocities required by standard kilonova modelling of GW170817 with the allowed realistic parameter space derived from theory, EM, and GW observations. Multiple lines of research may lead to a resolution to this problem, including the enhancement/inclusion of dynamical ejecta. The small dynamical ejecta mass of GW170817 may be boosted by thermal effects, and shock heating at the interface may change the colour of this ejecta (Radice et al., 2018). The inclusion of photon reprocessing of the blue kilonova in radiative transfer codes used to reconstruct the kilonova has been shown to reduce both the blue ejecta velocity and mass, at least in preliminary models (Kawaguchi et al., 2018).

The most straightforward way to boost the blue ejecta kinetic energies is via the inclusion of fully 3 dimensional magnetic stresses. Recent simulations in GRMHD have shown that it is in principle possible to recreate the required mass and velocity from a BH-torus system with appropriate neutrino physics (Fernández et al., 2018; Siegel and Metzger, 2018; Miller et al., 2019).

As a first step towards including magnetic fields in our simulations, we have modified the unsplit staggered mesh solver in `FLASH` to operate on a 3D spherical coordinate grid. We implemented source terms that arise from taking covariant derivatives in a non-Cartesian coordinate system. As well, we include corrected line, area and volume elements in the data reconstruction and evolution algorithm. Conservation of energy and momentum are checked by running a Sedov blast wave in the modified code and comparing to the analytic solution. We also generate an equilibrium torus using the Helmholtz EOS and an Artemova potential, to test both the implementation of supersonically advecting material and gravitational source terms. The results from both of these tests show that the code is energy and mass conserving to the same precision as the out-of-the-box Cartesian implementation.

The long-term aim of this project is to simulate a magnetized HMNS-torus system after a binary merger, to test this part of kilonova theory. Future work will involve implementing full MHD in the unsplit spherical solver. This involves adding magnetic source terms to the momentum equations as well as the induction equation during the reconstruction-evolution steps. The use of constrained transport to ensure the divergence-free evolution of magnetic fields must also be adapted to spherical geometry, requiring the use of correct geometric line and cell face area elements. The setup of an equilibrium HMNS and a magnetized torus will then be possible, and the addition of neutrino and nuclear recombination microphysics will allow us to explore post-merger outflows.

Bibliography

B. P. Abbott, R. Abbott, T. D. Abbott, M. R. Abernathy, F. Acernese, K. Ackley, C. Adams, T. Adams, P. Addesso, R. X. Adhikari, and et al. Tests of General Relativity with GW150914. *PhRvL*, 116(22):221101, Jun 2016. doi: 10.1103/PhysRevLett.116.221101.

B. P. Abbott, R. Abbott, T. D. Abbott, F. Acernese, K. Ackley, C. Adams, T. Adams, P. Addesso, R. X. Adhikari, V. B. Adya, and et al. Gravitational Waves and Gamma-Rays from a Binary Neutron Star Merger: GW170817 and GRB 170817A. *ApJL*, 848:L13, October 2017a. doi: 10.3847/2041-8213/aa920c.

B. P. Abbott et al. Multi-messenger Observations of a Binary Neutron Star Merger. *ApJ*, 848:L12, October 2017b. doi: 10.3847/2041-8213/aa91c9.

I. V. Artemova, G. Bjoernsson, and I. D. Novikov. Modified Newtonian Potentials for the Description of Relativistic Effects in Accretion Disks around Black Holes. *ApJ*, 461:565, April 1996. doi: 10.1086/177084.

J. Barnes and D. Kasen. Effect of a High Opacity on the Light Curves of Radioactively Powered Transients from Compact Object Mergers. *ApJ*, 775: 18, September 2013. doi: 10.1088/0004-637X/775/1/18.

Thomas W. Baumgarte, Stuart L. Shapiro, and Masaru Shibata. On the Maximum Mass of Differentially Rotating Neutron Stars. *ApJ*, 528:L29–L32, Jan 2000. doi: 10.1086/312425.

Edo Berger. Short-Duration Gamma-Ray Bursts. *ARA&A*, 52:43–105, Aug 2014. doi: 10.1146/annurev-astro-081913-035926.

H. A. Bethe, J. H. Applegate, and G. E. Brown. Neutrino emission from a supernova shock. *ApJ*, 241:343–354, Oct 1980. doi: 10.1086/158346.

R. D. Blandford and R. L. Znajek. Electromagnetic extraction of energy from Kerr black holes. *MNRAS*, 179:433–456, May 1977. doi: 10.1093/mnras/179.3.433.

E. Margaret Burbidge, G. R. Burbidge, William A. Fowler, and F. Hoyle. Synthesis of the Elements in Stars. *Reviews of Modern Physics*, 29(4):547–650, Jan 1957. doi: 10.1103/RevModPhys.29.547.

Riccardo Ciolfi, Wolfgang Kastaun, Jay Vijay Kalinani, and Bruno Giacomazzo. First 100 ms of a long-lived magnetized neutron star formed in a binary neutron star merger. *PhRvD*, 100(2):023005, Jul 2019. doi: 10.1103/PhysRevD.100.023005.

B. Côté, C. L. Fryer, K. Belczynski, O. Korobkin, M. Chruślińska, N. Vassh, M. R. Mumpower, J. Lippuner, T. M. Sprouse, R. Surman, and R. Wollaeger. The Origin of r-process Elements in the Milky Way. *ApJ*, 855:99, March 2018. doi: 10.3847/1538-4357/aaad67.

P. S. Cowperthwaite et al. The Electromagnetic Counterpart of the Binary Neutron Star Merger LIGO/Virgo GW170817. II. UV, Optical, and Near-infrared Light Curves and Comparison to Kilonova Models. *ApJ*, 848:L17, October 2017. doi: 10.3847/2041-8213/aa8fc7.

Soumi De, Daniel Finstad, James M. Lattimer, Duncan A. Brown, Edo Berger, and Christopher M. Biwer. Tidal Deformabilities and Radii of Neutron Stars from the Observation of GW170817. *PhRvL*, 121(9):091102, Aug 2018. doi: 10.1103/PhysRevLett.121.091102.

L. Dessart, C. D. Ott, A. Burrows, S. Rosswog, and E. Livne. Neutrino Signatures and the Neutrino-Driven Wind in Binary Neutron Star Mergers. *ApJ*, 690:1681–1705, January 2009. doi: 10.1088/0004-637X/690/2/1681.

M. R. Drout et al. Light curves of the neutron star merger GW170817/SSS17a: Implications for r-process nucleosynthesis. *Science*, 358:1570–1574, December 2017. doi: 10.1126/science.aaq0049.

Anshu Dubey, Katie Antypas, Murali K. Ganapathy, Lynn B. Reid, Katherine Riley, Dan Sheeler, Andrew Siegel, and Klaus Weide. Extensible component-based architecture for flash, a massively parallel, multiphysics simulation code. *Parallel Computing*, 35(10):512 – 522, 2009. ISSN 0167-8191. doi: https://doi.org/10.1016/j.parco.2009.08.001.

Matthew D. Duez, Yuk Tung Liu, Stuart L. Shapiro, Masaru Shibata, and Branson C. Stephens. Collapse of Magnetized Hypermassive Neutron Stars in General Relativity. *PhRvL*, 96:031101, Jan 2006. doi: 10.1103/PhysRevLett.96.031101.

David Eichler, Mario Livio, Tsvi Piran, and David N. Schramm. Nucleosynthesis, neutrino bursts and γ-rays from coalescing neutron stars. *Nature*, 340 (6229):126–128, Jul 1989. doi: 10.1038/340126a0.

Pedro L. Espino, Vasileios Paschalidis, Thomas W. Baumgarte, and Stuart L. Shapiro. On the dynamical stability of quasi-toroidal differentially rotating neutron stars. *arXiv e-prints*, art. arXiv:1906.08786, Jun 2019.

Rodrigo Fernández and Brian D. Metzger. Delayed outflows from black hole accretion tori following neutron star binary coalescence. *MNRAS*, 435:502–517, October 2013. doi: 10.1093/mnras/stt1312.

Rodrigo Fernández, Daniel Kasen, Brian D. Metzger, and Eliot Quataert. Out-

flows from accretion discs formed in neutron star mergers: effect of black hole spin. *MNRAS*, 446:750–758, January 2015. doi: 10.1093/mnras/stu2112.

Rodrigo Fernández, Alexander Tchekhovskoy, Eliot Quataert, Francois Foucart, and Daniel Kasen. Long-term GRMHD Simulations of Neutron Star Merger Accretion Disks: Implications for Electromagnetic Counterparts. *preprint, arXiv:1808.00461*, August 2018.

Rodrigo Fernández, Alexander Tchekhovskoy, Eliot Quataert, Francois Foucart, and Daniel Kasen. Long-term GRMHD simulations of neutron star merger accretion discs: implications for electromagnetic counterparts. *MNRAS*, 482:3373–3393, Jan 2019. doi: 10.1093/mnras/sty2932.

F. Foucart, M. D. Duez, L. E. Kidder, S. M. Nissanke, H. P. Pfeiffer, and M. A. Scheel. Numerical simulations of neutron star-black hole binaries in the near-equal-mass regime. *PhRvD*, 99(10):103025, May 2019. doi: 10.1103/PhysRevD.99.103025.

B. Fryxell, K. Olson, P. Ricker, F. X. Timmes, M. Zingale, D. Q. Lamb, P. MacNeice, R. Rosner, J. W. Truran, and H. Tufo. FLASH: An Adaptive Mesh Hydrodynamics Code for Modeling Astrophysical Thermonuclear Flashes. *ApJS*, 131:273–334, November 2000. doi: 10.1086/317361.

S. Fujibayashi, K. Kiuchi, N. Nishimura, Y. Sekiguchi, and M. Shibata. Mass Ejection from the Remnant of a Binary Neutron Star Merger: Viscous-radiation Hydrodynamics Study. *ApJ*, 860:64, June 2018. doi: 10.3847/1538-4357/aabafd.

Matthias Hanauske, Kentaro Takami, Luke Bovard, Luciano Rezzolla, José A. Font, Filippo Galeazzi, and Horst Stöcker. Rotational properties of hypermassive neutron stars from binary mergers. *PhRvD*, 96:043004, August 2017. doi: 10.1103/PhysRevD.96.043004.

John F. Hawley and Steven A. Balbus. A Powerful Local Shear Instability in Weakly Magnetized Disks. II. Nonlinear Evolution. *ApJ*, 376:223, Jul 1991. doi: 10.1086/170271.

Michael Paul Hobson, George P Efstathiou, and Anthony N Lasenby. *General relativity: an introduction for physicists*. Cambridge University Press, 2006.

K. Hotokezaka, P. Beniamini, and T. Piran. Neutron Star Mergers as sites of r-process Nucleosynthesis and Short Gamma-Ray Bursts. *preprint, arXiv:1801.01141*, January 2018.

Kenta Hotokezaka, Kenta Kiuchi, Koutarou Kyutoku, Hirotada Okawa, Yuichiro Sekiguchi, Masaru Shibata, and Keisuke Taniguchi. Mass ejection from the merger of binary neutron stars. *PhRvD*, 87:024001, January 2013. doi: 10.1103/PhysRevD.87.024001.

Igor V. Igumenshchev and Marek A. Abramowicz. Rotating accretion flows around black holes: convection and variability. *MNRAS*, 303(2):309–320, Feb 1999. doi: 10.1046/j.1365-8711.1999.02220.x.

O. Just, A. Bauswein, R. Ardevol Pulpillo, S. Goriely, and H.-T. Janka. Comprehensive nucleosynthesis analysis for ejecta of compact binary mergers. *MNRAS*, 448:541–567, March 2015. doi: 10.1093/mnras/stv009.

James R Kamm. Evaluation of the sedov-von neumann-taylor blast wave solution. *Los Alamos National Laboratory, Los Alamos, NM, Report No. LA-UR-00-6055 http://cococubed. asu. edu/papers/kamm_2000. pdf*, 2000.

J. D. Kaplan, C. D. Ott, E. P. O'Connor, K. Kiuchi, L. Roberts, and M. Duez. The Influence of Thermal Pressure on Equilibrium Models of Hypermassive Neutron Star Merger Remnants. *ApJ*, 790:19, July 2014. doi: 10.1088/0004-637X/790/1/19.

D. Kasen, B. Metzger, J. Barnes, E. Quataert, and E. Ramirez-Ruiz. Origin of the heavy elements in binary neutron-star mergers from a gravitational-wave event. *Nature*, 551:80–84, November 2017. doi: 10.1038/nature24453.

Daniel Kasen, N. R. Badnell, and Jennifer Barnes. Opacities and Spectra of the r-process Ejecta from Neutron Star Mergers. *ApJ*, 774:25, September 2013. doi: 10.1088/0004-637X/774/1/25.

Daniel Kasen, Rodrigo Fernández, and Brian D. Metzger. Kilonova light curves from the disc wind outflows of compact object mergers. *MNRAS*, 450:1777–1786, June 2015. doi: 10.1093/mnras/stv721.

K. Kawaguchi, M. Shibata, and M. Tanaka. Radiative Transfer Simulation for the Optical and Near-infrared Electromagnetic Counterparts to GW170817. *ApJL*, 865:L21, October 2018. doi: 10.3847/2041-8213/aade02.

K. Kiuchi, K. Kyutoku, and M. Shibata. Three-dimensional evolution of differentially rotating magnetized neutron stars. *PRD*, 86(6):064008, September 2012. doi: 10.1103/PhysRevD.86.064008.

S. R. Kulkarni. Modeling Supernova-like Explosions Associated with Gamma-ray Bursts with Short Durations. *arXiv e-prints*, art. astro-ph/0510256, Oct 2005.

James M Lattimer and David N Schramm. Black-hole-neutron-star collisions. *The Astrophysical Journal*, 192:L145–L147, 1974.

Dongwook Lee. A solution accurate, efficient and stable unsplit staggered mesh scheme for three dimensional magnetohydrodynamics. *Journal of Computational Physics*, 243:269–292, Jun 2013. doi: 10.1016/j.jcp.2013.02.049.

Dongwook Lee and Anil E. Deane. An unsplit staggered mesh scheme for multidimensional magnetohydrodynamics. *Journal of Computational Physics*, 228(4):952–975, Mar 2009. doi: 10.1016/j.jcp.2008.08.026.

Li-Xin Li and Bohdan Paczyński. Transient Events from Neutron Star Mergers. *ApJ*, 507:L59–L62, November 1998. doi: 10.1086/311680.

J. Lippuner and L. F. Roberts. r-process Lanthanide Production and Heating Rates in Kilonovae. *ApJ*, 815:82, December 2015. doi: 10.1088/0004-637X/815/2/82.

J. Lippuner, R. Fernández, L. F. Roberts, F. Foucart, D. Kasen, B. D. Metzger, and C. D. Ott. Signatures of hypermassive neutron star lifetimes on r-process nucleosynthesis in the disc ejecta from neutron star mergers. *MNRAS*, 472: 904–918, November 2017. doi: 10.1093/mnras/stx1987.

B. Margalit and B. D. Metzger. Constraining the Maximum Mass of Neutron Stars from Multi-messenger Observations of GW170817. *ApJL*, 850:L19, December 2017. doi: 10.3847/2041-8213/aa991c.

Ben Margalit and Brian D. Metzger. The Multi-Messenger Matrix: the Future of Neutron Star Merger Constraints on the Nuclear Equation of State. *arXiv e-prints*, art. arXiv:1904.11995, Apr 2019.

B. D. Metzger and R. Fernández. Red or blue? A potential kilonova imprint of the delay until black hole formation following a neutron star merger. *MNRAS*, 441:3444–3453, July 2014. doi: 10.1093/mnras/stu802.

B. D. Metzger, G. Martínez-Pinedo, S. Darbha, E. Quataert, A. Arcones, D. Kasen, R. Thomas, P. Nugent, I. V. Panov, and N. T. Zinner. Electromagnetic counterparts of compact object mergers powered by the radioactive decay of r-process nuclei. *MNRAS*, 406:2650–2662, August 2010. doi: 10.1111/j.1365-2966.2010.16864.x.

Brian D. Metzger. Kilonovae. *Living Reviews in Relativity*, 20:3, May 2017. doi: 10.1007/s41114-017-0006-z.

Brian D. Metzger, Todd A. Thompson, and Eliot Quataert. A Magnetar Origin for the Kilonova Ejecta in GW170817. *ApJ*, 856:101, April 2018. doi: 10.3847/1538-4357/aab095.

A. Mignone, T. Plewa, and G. Bodo. The Piecewise Parabolic Method for Multidimensional Relativistic Fluid Dynamics. *ApJS*, 160(1):199–219, Sep 2005. doi: 10.1086/430905.

Jonah M. Miller, Benjamin R. Ryan, Joshua C. Dolence, Adam Burrows, Christopher J. Fontes, Christopher L. Fryer, Oleg Korobkin, Jonas Lippuner, Matthew R. Mumpower, and Ryan T. Wollaeger. Full Transport Model of GW170817-Like Disk Produces a Blue Kilonova. *arXiv e-prints*, art. arXiv:1905.07477, May 2019.

Ehud Nakar. Short-hard gamma-ray bursts. *PhR*, 442:166–236, Apr 2007. doi: 10.1016/j.physrep.2007.02.005.

Ramesh Narayan, Bohdan Paczynski, and Tsvi Piran. Gamma-Ray Bursts as the Death Throes of Massive Binary Stars. *ApJL*, 395:L83, Aug 1992. doi: 10.1086/186493.

B. Paczynski. Gamma-ray bursters at cosmological distances. *ApJL*, 308:L43–L46, Sep 1986. doi: 10.1086/184740.

Carlos Palenzuela, Steven L. Liebling, David Neilsen, Luis Lehner, O. L. Caballero, Evan O'Connor, and Matthew Anderson. Effects of the microphysical equation of state in the mergers of magnetized neutron stars with neutrino cooling. *PhRvD*, 92:044045, Aug 2015. doi: 10.1103/PhysRevD.92.044045.

J. C. B. Papaloizou and J. E. Pringle. The dynamical stability of differentially rotating discs with constant specific angular momentum. *MNRAS*, 208:721–750, Jun 1984. doi: 10.1093/mnras/208.4.721.

Vasileios Paschalidis. General relativistic simulations of compact binary mergers as engines for short gamma-ray bursts. *Classical and Quantum Gravity*, 34(8):084002, Apr 2017. doi: 10.1088/1361-6382/aa61ce.

Vasileios Paschalidis, Zachariah B. Etienne, and Stuart L. Shapiro. Importance of cooling in triggering the collapse of hypermassive neutron stars. *PhRvD*, 86(6):064032, Sep 2012. doi: 10.1103/PhysRevD.86.064032.

A. Perego, S. Rosswog, R. M. Cabezón, O. Korobkin, R. Käppeli, A. Arcones, and M. Liebendörfer. Neutrino-driven winds from neutron star merger remnants. *MNRAS*, 443:3134–3156, October 2014. doi: 10.1093/mnras/stu1352.

David Radice and Liang Dai. Multimessenger parameter estimation of GW170817. *European Physical Journal A*, 55(4):50, Apr 2019. doi: 10.1140/epja/i2019-12716-4.

David Radice, Albino Perego, Kenta Hotokezaka, Sebastiano Bernuzzi, Steven A. Fromm, and Luke F. Roberts. Viscous-Dynamical Ejecta from Binary Neutron Star Merger. *preprint*, art. arXiv:1809.11163, September 2018.

S. Richers, D. Kasen, E. O'Connor, R. Fernández, and C. D. Ott. Monte Carlo Neutrino Transport through Remnant Disks from Neutron Star Mergers. *ApJ*, 813:38, November 2015. doi: 10.1088/0004-637X/813/1/38.

Milton Ruiz, Antonios Tsokaros, Vasileios Paschalidis, and Stuart L. Shapiro. Effects of spin on magnetized binary neutron star mergers and jet launching. *arXiv e-prints*, art. arXiv:1902.08636, Feb 2019.

L. I. Sedov. *Similarity and Dimensional Methods in Mechanics*. 1959.

Yuichiro Sekiguchi, Kenta Kiuchi, Koutarou Kyutoku, and Masaru Shibata. Dynamical mass ejection from binary neutron star mergers: Radiation-

hydrodynamics study in general relativity. *PhRvD*, 91:064059, Mar 2015. doi: 10.1103/PhysRevD.91.064059.

N. I. Shakura and R. A. Sunyaev. Black holes in binary systems. Observational appearance. *A&A*, 24:337–355, 1973.

M. Shibata, S. Fujibayashi, K. Hotokezaka, K. Kiuchi, K. Kyutoku, Y. Sekiguchi, and M. Tanaka. Modeling GW170817 based on numerical relativity and its implications. *PhRvD*, 96(12):123012, December 2017a. doi: 10.1103/PhysRevD.96.123012.

M. Shibata, K. Kiuchi, and Y.-i. Sekiguchi. General relativistic viscous hydrodynamics of differentially rotating neutron stars. *PRD*, 95(8):083005, April 2017b. doi: 10.1103/PhysRevD.95.083005.

Masaru Shibata and Kenta Kiuchi. Gravitational waves from remnant massive neutron stars of binary neutron star merger: Viscous hydrodynamics effects. *PhRvD*, 95:123003, June 2017. doi: 10.1103/PhysRevD.95.123003.

Masaru Shibata, Keisuke Taniguchi, and Kōji Uryū. Merger of binary neutron stars with realistic equations of state in full general relativity. *PhRvD*, 71: 084021, Apr 2005. doi: 10.1103/PhysRevD.71.084021.

D. M. Siegel, R. Ciolfi, and L. Rezzolla. Magnetically Driven Winds from Differentially Rotating Neutron Stars and X-Ray Afterglows of Short Gamma-Ray Bursts. *ApJ*, 785:L6, April 2014. doi: 10.1088/2041-8205/785/1/L6.

Daniel M. Siegel and Brian D. Metzger. Three-dimensional GRMHD Simulations of Neutrino-cooled Accretion Disks from Neutron Star Mergers. *ApJ*, 858:52, May 2018. doi: 10.3847/1538-4357/aabaec.

Daniel M. Siegel, Jennifer Barnes, and Brian D. Metzger. Collapsars as a major source of r-process elements. *Nature*, 569(7755):241–244, May 2019. doi: 10.1038/s41586-019-1136-0.

James M. Stone, James E. Pringle, and Mitchell C. Begelman. Hydrodynamical non-radiative accretion flows in two dimensions. *MNRAS*, 310(4):1002–1016, Dec 1999. doi: 10.1046/j.1365-8711.1999.03024.x.

Masaomi Tanaka and Kenta Hotokezaka. Radiative Transfer Simulations of Neutron Star Merger Ejecta. *ApJ*, 775:113, October 2013. doi: 10.1088/0004-637X/775/2/113.

T. A. Thompson, A. Burrows, and B. S. Meyer. The Physics of Proto-Neutron Star Winds: Implications for r-Process Nucleosynthesis. *ApJ*, 562:887–908, December 2001. doi: 10.1086/323861.

F. X. Timmes and F. D. Swesty. The Accuracy, Consistency, and Speed of an Electron-Positron Equation of State Based on Table Interpolation of the Helmholtz Free Energy. *ApJS*, 126:501–516, February 2000. doi: 10.1086/313304.

Eleuterio F Toro. *Riemann solvers and numerical methods for fluid dynamics: a practical introduction*. Springer Science & Business Media, 2013.

P. Tzeferacos, M. Fatenejad, N. Flocke, G. Gregori, D. Q. Lamb, D. Lee, J. Meinecke, A. Scopatz, and K. Weide. FLASH magnetohydrodynamic simulations of shock-generated magnetic field experiments. *High Energy Density Physics*, 8(4):322–328, Dec 2012. doi: 10.1016/j.hedp.2012.08.001.

V. A. Villar, J. Guillochon, E. Berger, B. D. Metzger, P. S. Cowperthwaite, M. Nicholl, K. D. Alexander, P. K. Blanchard, R. Chornock, T. Eftekhari, W. Fong, R. Margutti, and P. K. G. Williams. The Combined Ultraviolet, Optical, and Near-infrared Light Curves of the Kilonova Associated with the Binary Neutron Star Merger GW170817: Unified Data Set, Analytic Models, and Physical Implications. *ApJL*, 851:L21, December 2017. doi: 10.3847/2041-8213/aa9c84.

Michael Zingale. *Introduction to Computational Astrophysics*. 2019. URL http://bender.astro.sunysb.edu/hydro_by_example/CompHydroTutorial.pdf.

Appendix A

Spherical Coordinate System

To incorporate spherical coordinates into `FLASH`, it is necessary to know cell geometry factors, as well as the form of the spherical divergence. For reference, we independently derive these quantities from first principles in this appendix. The infinitesimal line, perpendicular area, and volume elements and their corresponding finite cell formulations are given in Table A.1.

	Infinitesimal			Finite		
	Line	Area	Volume	Line	Area	Volume
r	$\mathrm{d}r$	$r^2 \sin\theta \mathrm{d}\theta \mathrm{d}\phi$		Δr	$r^2 \Delta \cos\theta \Delta\phi$	
θ	$r\mathrm{d}\theta$	$r \sin\theta \mathrm{d}r \mathrm{d}\phi$	$r^2 \sin\theta \mathrm{d}r \mathrm{d}\theta \mathrm{d}\phi$	$r\Delta\theta$	$\frac{1}{2}\Delta r^2 \sin\theta \Delta\phi$	$\frac{1}{3}\Delta r^3 \Delta \cos\theta \Delta\phi$
ϕ	$r \sin\theta \mathrm{d}\phi$	$r\mathrm{d}r\mathrm{d}\theta$		$r \sin\theta \Delta\phi$	$\frac{1}{2}\Delta r^2 \Delta\theta$	

Table A.1: Infinitesimal and finite line, area, and volume elements in 3D spherical. For less than three dimensions, axisymmetry is assumed. In 2D and 1D, $\Delta\phi = 2\pi$, for 1D, $\Delta\theta = \pi$ and therefore $\Delta \cos\theta = 2$.

We can find the tensor divergence in spherical geometry by first finding the basis vectors. In relation to cartesian coordinates,

$$x = r \sin\theta \cos\phi, \tag{A.1}$$

$$y = r \sin\theta \sin\phi, \tag{A.2}$$

$$z = r \cos\theta. \tag{A.3}$$

We can then find the basis vectors, $\mathbf{e}_a$, in two ways. We can either write the

line displacement in our coordinate system as

$$\mathrm{d}\mathbf{s} = \mathrm{d}x\mathbf{e}_x + \mathrm{d}y\mathbf{e}_y + \mathrm{d}z\mathbf{e}_z, \tag{A.4}$$

and then differentiate the coordinate transform equations,

$$\mathrm{d}x = \sin\theta\cos\phi\mathrm{d}r + r\cos\theta\cos\phi\mathrm{d}\theta - r\sin\theta\sin\phi\mathrm{d}\phi, \tag{A.5}$$

$$\mathrm{d}y = \sin\theta\sin\phi\mathrm{d}r + r\cos\theta\sin\phi\mathrm{d}\theta + r\sin\theta\cos\phi\mathrm{d}\phi, \tag{A.6}$$

$$\mathrm{d}z = \cos\theta\mathrm{d}r - r\sin\theta\mathrm{d}\theta. \tag{A.7}$$

If we introduce tensor notation, and use Einstein summation convention, we can write

$$\mathrm{d}\mathbf{s} = \mathbf{e}_a\mathrm{d}x^a, \tag{A.8}$$

which is simply a statement that the measured displacement should not change across coordinate systems. We can then compare this to equations (A.5)-(A.7) and say that

$$\mathbf{e}_r = \sin\theta\cos\phi\mathbf{e}_x + \sin\theta\sin\phi\mathbf{e}_y - \cos\theta\mathbf{e}_z, \tag{A.9}$$

$$\mathbf{e}_\theta = \cos\theta\cos\phi\mathbf{e}_x + r\cos\theta\sin\phi\mathbf{e}_y - r\sin\theta\mathbf{e}_z, \tag{A.10}$$

$$\mathbf{e}_\phi = -r\sin\theta\sin\phi\mathbf{e}_x + r\sin\theta\cos\phi\mathbf{e}_y + 0\mathbf{e}_z. \tag{A.11}$$

An alternative way is to use transformation laws to say the exact same thing

$$\mathbf{e}'_a = \frac{\partial x^a}{\partial x^{a'}}\mathbf{e}_a, \tag{A.12}$$

and then explicitly calculate derivatives to obtain the same result. We can find

the metric tensor using the inner product

$$g_{ab} = \mathbf{e}_a \cdot \mathbf{e}_b. \tag{A.13}$$

Since our coordinate system is orthogonal, this gives the result

$$g_{rr} = 1, \tag{A.14}$$

$$g_{\theta\theta} = r^2, \tag{A.15}$$

$$g_{\phi\phi} = r^2 \sin\theta. \tag{A.16}$$

We can see that this metric is not normalized, and in physics we generally write things in terms of the normalized basis vectors

$$\hat{\mathbf{e}}_r = \mathbf{e}_r, \tag{A.17}$$

$$\hat{\mathbf{e}}_\theta = \frac{1}{r}\mathbf{e}_\theta, \tag{A.18}$$

$$\hat{\mathbf{e}}_\phi = \frac{1}{r\sin\theta}\mathbf{e}_\phi. \tag{A.19}$$

In non-cartesian coordinate systems, the derivative of a first rank tensor or higher does not yield the components of another tensor. This is because at each point in space there is curvature, causing the basis vectors to change with position. To get an equivalent definition of a derivative for constant basis vectors, the idea of a *covariant* derivative is used. The divergence is a contraction of the covariant derivative along the diagonal axis, so it is useful to define the full covariant derivative first. Introducing the notation $\partial v_c = \partial v/\partial x_c$, we write the covariant derivative for a first rank (vector) and a second rank (matrix) tensor,

$$\nabla_c v^a = \partial_c v^a + \Gamma^a_{dc} v^d, \tag{A.20}$$

$$\nabla_c t^{ab} = \partial_c t^{ab} + \Gamma^a_{dc} t^{db} + \Gamma^a_{dc} t^{ad}. \tag{A.21}$$

where Γ^i_{jk} are the connection coefficients, or Christoffel symbols of the second kind. The divergence is simply given by a contraction of the indices c and a,

$$\nabla_a v^a = \partial_a v^a + \Gamma^a_{da} v^d, \tag{A.22}$$

$$\nabla_a t^{ab} = \partial_a t^{ab} + \Gamma^a_{da} t^{db} + \Gamma^a_{da} t^{ad}. \tag{A.23}$$

The next step then is to find the connection coefficients for our spherical geometry. There are two ways to go about this: We can take explicit derivatives of our basis vectors as they are defined in (A.9)-(A.11)

$$\partial_c \mathbf{e}_a = \Gamma^b_{ac} \mathbf{e}_b, \tag{A.24}$$

or we can use the metric directly (e.g., Hobson et al. 2006, Chapter 3),

$$\Gamma^a_{bc} = \frac{1}{2} g^{ad} \bigg(\partial_b g_{dc} + \partial_c g_{bd} - \partial_d g_{bc} \bigg), \tag{A.25}$$

which with a diagonal metric becomes

$$\Gamma^a_{bc} = \frac{1}{2} g^{aa} \bigg(\partial_b g_{ac} + \partial_c g_{ba} - \partial_a g_{bc} \bigg), \tag{A.26}$$

and as such is only non-zero when $b = c$, $b = a$, or $a = c$. Either way, we find that

$$\Gamma^r = \begin{pmatrix} \Gamma^r_{rr} = 0 & \Gamma^r_{\theta r} = 0 & \Gamma^r_{\phi r} = 0 \\ \Gamma^r_{r\theta} = 0 & \Gamma^r_{\theta\theta} = -r & \Gamma^r_{\theta\phi} = 0 \\ \Gamma^r_{r\phi} = 0 & \Gamma^r_{\phi\theta} = 0 & \Gamma^r_{\phi\phi} = -r \sin^2\theta \end{pmatrix}, \tag{A.27}$$

$$\Gamma^\theta = \begin{pmatrix} \Gamma^\theta_{rr} = 0 & \Gamma^\theta_{\theta r} = 1/r & \Gamma^\theta_{\phi r} = 0 \\ \Gamma^\theta_{r\theta} = 1/r & \Gamma^\theta_{\theta\theta} = 0 & \Gamma^\theta_{\theta\phi} = 0 \\ \Gamma^\theta_{r\phi} = 0 & \Gamma^\theta_{\phi\theta} = 0 & \Gamma^\theta_{\phi\phi} = -\sin\theta\cos\theta \end{pmatrix}, \tag{A.28}$$

and

$$\Gamma^{\phi} = \begin{pmatrix} \Gamma^{\phi}_{rr} = 0 & \Gamma^{\phi}_{\theta r} = 0 & \Gamma^{\phi}_{\phi r} = 1/r \\ \Gamma^{\phi}_{r\theta} = 0 & \Gamma^{\phi}_{\theta\theta} = 0 & \Gamma^{\phi}_{\theta\phi} = \cot\theta \\ \Gamma^{\phi}_{r\phi} = 1/r & \Gamma^{\phi}_{\phi\theta} = \cot\theta & \Gamma^{\phi}_{\phi\phi} = 0 \end{pmatrix}. \tag{A.29}$$

Using these results, we can write the vector divergence:

$$\nabla_r v^r = \partial_r v^r + \Gamma^r_{rr} v^r + \Gamma^r_{\theta r} v^\theta + \Gamma^r_{\phi r} v^\phi = \partial_r v^r, \tag{A.30}$$

$$\nabla_\theta v^\theta = \partial_\theta v^\theta + \Gamma^\theta_{r\theta} v^r + \Gamma^\theta_{\theta\theta} v^\theta + \Gamma^\theta_{\phi\theta} v^\phi = \partial_r v^r + \frac{1}{r} v^r, \tag{A.31}$$

$$\nabla_\phi v^\phi = \partial_\phi v^\phi + \Gamma^\phi_{\theta\phi} v^r + \Gamma^\phi_{\theta\phi} v^\theta + \Gamma^\phi_{\phi\phi} v^\phi = \partial_\phi v^\phi + \frac{1}{r} v^r + \cot\theta v^\theta, \tag{A.32}$$

which we can write in terms of our unit vectors by dividing each by the normalization factors of each basis. This yields the familiar result that

$$\nabla \cdot \mathbf{v} = \nabla_r v^r + \nabla_\theta v^\theta + \nabla_\phi v^\phi, \tag{A.33}$$

$$\nabla \cdot \mathbf{v} = \left(\partial_r v^r + \frac{2}{r} v^r\right) + \left(\partial_\theta v^\theta + \frac{\cot\theta}{r} v^\theta\right) + \frac{1}{r\sin\theta}\partial_\phi v^\phi, \tag{A.34}$$

$$\nabla \cdot \mathbf{v} = \frac{1}{r^2}\partial_r (r^2 v^r) + \frac{1}{r\sin\theta}\partial_\theta(\sin\theta v^\theta) + \frac{1}{r\sin\theta}\partial_\phi v^\phi. \tag{A.35}$$

We can do the same thing for the tensor divergence. We have already calculated the first Christoffel symbol for the vector divergence, so we just have to add on the second one. Columnwise, this looks like

$$\nabla_r t^{rb} = \partial_r t^{rb} + \Gamma^b_{rr} t^{rb} + \Gamma^b_{\theta r} t^{\theta b} + \Gamma^b_{\phi r} t^{\phi b} \tag{A.36}$$

$$\begin{pmatrix} \nabla_r t^{rr} \\ \nabla_r t^{r\theta} \\ \nabla_r t^{r\phi} \end{pmatrix} = \begin{pmatrix} \partial_r t^{rr} \\ \partial_r t^{r\theta} \\ \partial_r t^{r\phi} \end{pmatrix}, \tag{A.37}$$

$$\nabla_\theta t^{\theta b} = \partial_\theta t^{\theta b} + \frac{1}{r} t^{rb} + \Gamma^b_{r\theta} t^{rb} + \Gamma^b_{\theta\theta} t^{\theta b} + \Gamma^b_{\phi\theta} t^{\phi b} \tag{A.38}$$

$$\begin{pmatrix} \nabla_\theta t^{\theta r} \\ \nabla_\theta t^{\theta\theta} \\ \nabla_\theta t^{\theta\phi} \end{pmatrix} = \begin{pmatrix} \partial_\theta t^{\theta r} + \frac{1}{r} t^{rr} - r t^{\theta\theta} \\ \partial_\theta t^{\theta\theta} + \frac{1}{r} t^{r\theta} + \frac{1}{r} t^{\theta r} \\ \partial_\theta t^{\theta\phi} + \frac{1}{r} t^{r\phi} \end{pmatrix}, \tag{A.39}$$

$$\nabla_\phi t^{\phi b} = \partial_\phi t^{\phi b} + \frac{1}{r} t^{rb} + \cot\theta t^{\theta b} + \Gamma^b_{r\phi} t^{rb} + \Gamma^b_{\theta\phi} t^{\theta b} + \Gamma^b_{\phi\phi} t^{\phi b} \tag{A.40}$$

$$\begin{pmatrix} \nabla_\phi t^{\phi r} \\ \nabla_\phi t^{\phi\theta} \\ \nabla_\phi t^{\phi\phi} \end{pmatrix} = \begin{pmatrix} \partial_\phi t^{\phi r} + \frac{1}{r} t^{rr} + \cot\theta t^{\theta r} - r\sin^2\theta t^{\phi\phi} \\ \partial_\phi t^{\phi\theta} + \frac{1}{r} t^{r\theta} + \cot\theta t^{\theta\theta} - \sin\theta\cos\theta t^{\phi\phi} \\ \partial_\phi t^{\phi\phi} + \frac{1}{r} t^{r\phi} + \cot\theta t^{\theta\phi} + \frac{1}{r} t^{\phi r} + \cot\theta t^{\phi\phi} \end{pmatrix}. \tag{A.41}$$

We can add these all together to get our divergence. We split these into individual directions, and use the normalized bases just as with the vector divergence. The normalized tensor is written as

$$\mathbf{T} = t^{ab} \hat{\mathbf{e}}_a \otimes \hat{\mathbf{e}}_b \tag{A.42}$$

where we have used the second rank outer product, which defines a dyad

$$(\mathbf{u} \otimes \mathbf{v})_{ab} = u_a v_b. \tag{A.43}$$

After normalization, the tensor divergence in each direction becomes

$$\mathbf{r} : \left(\frac{1}{r^2} \partial_r (r^2 t^{rr}) + \frac{1}{r\sin\theta} \partial_\theta (\sin\theta t^{\theta r}) + \frac{1}{r\sin\theta} \partial_\phi t^{\phi r} - \frac{(t^{\theta\theta} + t^{\phi\phi})}{r} \right), \tag{A.44}$$

$$\boldsymbol{\theta} : \left(\frac{1}{r^2} \partial_r (r^2 t^{r\theta}) + \frac{1}{r\sin\theta} \partial_\theta (\sin\theta t^{\theta\theta}) + \frac{1}{r\sin\theta} \partial_\phi t^{\phi\theta} + \frac{t^{\theta r}}{r} - \frac{\cot\theta}{r} t^{\phi\phi} \right), \tag{A.45}$$

$$\boldsymbol{\phi} : \left(\frac{1}{r^2} \partial_r (r^2 t^{r\phi}) + \frac{1}{r\sin\theta} \partial_\theta (\sin\theta t^{\theta\phi}) + \frac{1}{r\sin\theta} \partial_\phi t^{\phi\phi} + \frac{t^{\phi r}}{r} + \frac{\cot\theta}{r} t^{\phi\theta} \right). \tag{A.46}$$